



NICER/NuSTAR Characterization of 4U 1957+11: A Near Maximally Spinning Black Hole Potentially in the Mass Gap

Erin Barillier^{1,2}, Victoria Grinberg³, David Horn⁴, Michael A. Nowak¹, Ronald A. Remillard⁵, James F. Steiner⁶,
Dominic J. Walton^{7,8}, and Jörn Wilms⁹

¹ Physics Department, CB 1105, Washington University, One Brookings Drive, St. Louis, MO 63130-4899, USA; erinbari@umich.edu, mnowak@physics.wustl.edu

² Department of Physics, Randall Lab, University of Michigan, 450 Church Street, Ann Arbor, MI 48109-1040, USA

³ European Space Agency (ESA), European Space Research and Technology Centre (ESTEC), Keplerlaan 1, 2201 AZ Noordwijk, The Netherlands
victoria.grinberg@esa.int

⁴ Dr. Karl Remeis-Observatory & ECAP, Friedrich-Alexander-Universität Erlangen-Nürnberg, Sternwartstr. 7, D-96049 Bamberg, Germany; david.horn@fau.de

⁵ MIT Kavli Institute for Astrophysics and Space Research, Cambridge, MA 02139, USA; ronr@gmail.com

⁶ Center for Astrophysics—Harvard & Smithsonian, 60 Garden Street, Cambridge, MA 02138, USA; james.steiner@cfa.harvard.edu

⁷ Centre for Astrophysics Research, University of Hertfordshire, College Lane, Hatfield AL10 9AB, UK; walton@ast.cam.ac.uk

⁸ Institute of Astronomy, University of Cambridge, Madingley Road, Cambridge CB3 0HA, UK

⁹ Dr. Karl Remeis-Observatory & ECAP, Friedrich-Alexander-Universität Erlangen-Nürnberg, Sternwartstr. 7, D-96049 Bamberg, Germany
joern.wilms@sternwarte.uni-erlangen.de

Received 2022 October 24; revised 2022 December 14; accepted 2022 December 19; published 2023 February 22

Abstract

4U 1957+11 is a black hole candidate system that has been in a soft X-ray spectral state since its discovery. We present analyses of recent joint NICER and NuSTAR spectra, which are extremely well described by a highly inclined disk accreting into a near maximally spinning black hole. Owing to the broad X-ray coverage of NuSTAR, the fitted spin and inclination are strongly constrained for our hypothesized disk models. The faintest spectra are observed out to 20 keV, even though their hard tail components are almost absent when described with a simple corona. The hard tail increases with luminosity, but shows clear two-track behavior with one track having appreciably stronger tails. The disk spectrum color-correction factor is anticorrelated with the strength of the hard tail (e.g., as measured by the Compton y parameter). Although the spin and inclination parameters are strongly constrained for our chosen model, the mass and distance are degenerate parameters. We use our spectral fits, along with a theoretical prior on color-correction, an observational prior on likely fractional Eddington luminosity, and an observational prior on distance obtained from Gaia studies, to present mass and distance contours for this system. The most likely parameters, given our presumed disk model, suggest a $4.6 M_{\odot}$ black hole at 7.8 kpc observed at luminosities ranging from $\approx 1.7\%$ to 9% of Eddington. This would place 4U 1957+11 as one of the few actively accreting sources within the *mass gap* of $\approx 2\text{--}5 M_{\odot}$ where there are few known massive neutron stars or low-mass black holes. Higher mass and distance, however, remain viable.

Unified Astronomy Thesaurus concepts: Kerr black holes (886); Low-mass x-ray binary stars (939); Accretion (14); X-ray sources (1822); Stellar mass black holes (1611); X-ray astronomy (1810); Gamma-ray astronomy (628); Relativistic disks (1388); Distance measure (395)

1. Introduction

Most of the known systems in our galaxy suspected of harboring a stellar mass black hole were discovered via observations of X-ray binary systems that have undergone one or more transient outbursts. The list of persistently X-ray bright black hole candidate systems is somewhat shorter, with some of the brightest sources comprised of systems with high-mass ($\gtrsim 3 M_{\odot}$) secondaries, e.g., Cyg X-1 (black hole mass $21.2^{+2.2}_{-2.3} M_{\odot}$, companion mass $40.6^{+7.7}_{-7.1} M_{\odot}$; Miller-Jones et al. 2021), LMC X-3 (black hole mass $7.0 \pm 0.6 M_{\odot}$, companion mass $3.6 \pm 0.6 M_{\odot}$; Orosz et al. 2014), and LMC X-1 (black hole mass $10.9 \pm 1.4 M_{\odot}$, companion mass $31.8 \pm 3.5 M_{\odot}$; Orosz et al. 2009). These three systems also spend a significant fraction of their time in a soft X-ray spectral state (ranging from $\gtrsim 20\%$ of the time in the case of Cyg X-1, Grinberg et al. 2013, to 100% in the case of LMC X-1). 4U 1957+11 is a low-mass X-ray binary (LMXB) system, with comparable observed

brightness to LMC X-1 and LMC X-3, that is also thought to harbor a black hole (Margon et al. 1978; Thorstensen 1987; Hakala et al. 1999). Also similar to the above high-mass X-ray binary (HMXB) sources, it has frequently been observed in a soft X-ray spectral state, and in fact has never been identified with a hard X-ray spectral state (e.g., Yaqoob et al. 1993; Ricci et al. 1995; Nowak et al. 1999; Wijnands et al. 2002; Nowak et al. 2012; Maitra et al. 2014; Maccarone et al. 2020). Unfortunately, partly owing to its persistent nature, and thereby not allowing optical measurements of binary parameters in quiescence, little is known about the system’s mass, distance, and inclination. Mass estimates in particular have ranged from hypothesizing a neutron star primary (Bayless et al. 2011) all the way to suggesting a black hole of possibly tens of solar masses (Nowak et al. 2012).

4U 1957+11 exhibits a 9.33 hr optical orbital period (Thorstensen 1987), which would be indicative of a low-mass companion ($\lesssim 1 M_{\odot}$) if Roche Lobe overflow supplies accretion from a secondary with a radius equal to or greater than that expected for a main-sequence star. Optical emission is likely dominated by the accretion disk (Hakala et al. 2014); however, numerous analyses have attributed observed $\pm 20\%$ optical modulation to irradiation–heating of the surface of the

secondary (Bayless et al. 2011; Mason et al. 2012; Gomez et al. 2015). Requiring that irradiation of the secondary be primarily responsible for the optical modulation suggests that the secondary subtends a significant fraction of the sky from the primary’s point of view. Thus the binary system would have a small total mass, perhaps most consistent with a neutron star primary¹⁰ or low-mass black hole (Bayless et al. 2011; Gomez et al. 2015). These optical models also allow for a range of system inclinations (e.g., Bayless et al. 2011 fit inclinations ranging from 20° to 70°). On the other hand, Hakala et al. (2014) model the optical spectral energy distribution as being due to X-ray heating of the outer accretion disk and, based upon these models, argue for a distance of at least 15 kpc and a commensurately large mass $>15 M_{\odot}$. Furthermore, the high modulation amplitudes and complex orbital structure possibly seen in some optical observations have been attributed to the heating of the outer edge of a disk seen at large (but not eclipsing) inclination angles (Hakala et al. 1999; Russell et al. 2010).

It is known from modeling both cold and hot phase interstellar medium (ISM) absorption along the line of sight to 4U 1957+11 that it resides outside of the plane of the galaxy at a minimum distance of $\gtrsim 5$ kpc (Nowak et al. 2008; Yao et al. 2008). Lying within the Galactic halo means that any prior radio jet activity from 4U 1957+11 has not interacted with a dense ISM and therefore has not produced a nearby radio *hot spot* that can be confused with current jet emission. This has allowed the most stringent upper limits to be placed upon the ratio of radio to X-ray flux during a black hole “soft state” (Russell et al. 2011; Maccarone et al. 2020).

Maccarone et al. (2020) also consider a variety of other optical observations of 4U 1957+11, including spectroscopic studies of Bowen fluorescence lines (Longa-Peña 2015) and parallax and proper-motion studies using the Gaia EDR3 catalog (Gaia Collaboration et al. 2016, 2021), to evaluate distance, mass, and potential kick velocity constraints (assuming a Galactic halo orbit) for this system. Their most important constraint is that Gaia results are consistent with a median distance of 7 kpc with a 95% likely range of 3–15 kpc. Depending upon specific assumptions, these measurements suggest that 4U 1957+11 may be the fastest moving black hole system known in the galaxy, but its mass remains ambiguous. If the Bowen fluorescence line studies (Longa-Peña 2015) are taken at face value, then the mass ratio in the system is ≈ 0.25 – 0.3 , arguing for a low-mass black hole or high-mass neutron star system.

Studies based solely upon X-ray observations have been no more definitive. All studies agree that the soft X-ray spectrum is consistent with emission from an accretion disk (e.g., Mitsuda et al. 1984) with a high peak temperature and low normalization (see Nowak et al. 2012; Maitra et al. 2014). Such a high temperature–low normalization can be achieved by combinations of low mass, high spin, and high accretion rate for a black hole accreting from a disk being viewed at high inclination and/or large distance, but degeneracies in the model fits abound (Nowak et al. 2012; Maitra et al. 2014). The lack of X-ray eclipses by the Roche lobe of the secondary limits the

disk model inclinations to $\lesssim 80^{\circ}$ (for a $1 M_{\odot}$ secondary), but otherwise allows a wide range of parameters.

Taken as a whole, the optical and X-ray results to date allow for, but do not strictly require, the compact object in 4U 1957+11 to be a low-mass black hole residing in the “mass gap” of ≈ 2 – $5 M_{\odot}$ (Farr et al. 2011), which approximately spans from the masses of the most massive known neutron stars to the least massive known black holes. Few compact objects, especially those that have exhibited active accretion, have been found within this mass range. It has been argued that the maximum mass of a neutron star is *at least* $2.19 M_{\odot}$ (1σ confidence, based upon a $2.35 \pm 0.17 M_{\odot}$ mass estimate for PSR J0952–0607, as well as high mass estimates for several other well-observed systems; Romani et al. 2022). For low-mass black holes, several noninteracting binaries have been claimed to harbor black holes with likely masses $<5 M_{\odot}$ ($3.3^{+2.8}_{-0.7} M_{\odot}$ for 2MASS J05215658+4359220, Thompson et al. 2019, 2020; $4.53 \pm 0.21 M_{\odot}$ and $4.4 \pm 2.8 M_{\odot}$ in the globular cluster NGC 3201, Giesers et al. 2018, 2019; or Shenar et al. 2022, who identify ten O-star binaries, out of a sample of fifty one, that might harbor black holes with masses $<5 M_{\odot}$). Among at least intermittently active X-ray binaries, XTE J1650–500 could have an upper mass limit of $\approx 4 M_{\odot}$ if the accretion disk contributes significantly to the optical lightcurve of the system (Orosz et al. 2004). Thus it would be extremely interesting if observations could determine whether or not 4U 1957+11 is another example of a low-mass black hole system, in this case a persistently accreting one.

The goal of this work is to consider a new set of X-ray data¹¹ for 4U 1957+11, and consider them along with Gaia optical constraints comparable to those discussed by Maccarone et al. (2020). We further include considerations of theoretical disk modeling and observational X-ray properties for other known black hole systems in order to reassess constraints on the mass and distance of the 4U 1957+11 system. As we discuss below, what makes these Nuclear Spectroscopic Telescope Array (NuSTAR) observations of 4U 1957+11 unique is that they extend to energies of 20 keV or beyond, with high signal-to-noise and minimal background uncertainties. This allows more precise fitting of disk models than we have achieved with previous studies. Here we find that the 4U 1957+11 spectra are in a regime with minimal degeneracy with regards to the fitted spin and inclination for the relativistic disk models that we have chosen to consider (see Parker et al. 2019).

The outline of the paper is as follows. In Section 2, we place the historical behavior of 4U 1957+11 in context in relation to other well-observed black hole systems by presenting a variation of color-intensity diagrams created from Rossi X-ray Timing Explorer (RXTE) observations. In Section 3, we describe the newer X-ray observations from NuSTAR and Neutron Star Interior Composition Explorer (NICER) that we utilize in this work. Sections 4 and 5 describe variability analyses (including consideration of the Monitor of All-sky X-ray Image, hereafter MAXI, lightcurves for 4U 1957+11) and spectral analyses of these data, respectively. Included with our discussion of the spectral fits, we consider in Section 5.1 the scaling relationships that describe degeneracies of the fit parameters. We then summarize our conclusions in Section 6.

¹⁰ The main argument against a neutron star primary has been the lack of nuclear bursts, pulsar signatures, or the need for any “surface emission” component in any analysis of X-ray spectra for all the observations that have been performed to date, including those presented in this work.

¹¹ Of the ten NuSTAR observations discussed herein, however, nine have previously been presented by Sharma et al. (2021), and one has been presented by Mudambi et al. (2022). None of the joint NICER observations were discussed in either of those works.

2. 4U 1957+11 *q*-diagram

It has been known for nearly thirty years that at low luminosities black hole systems tend to be in a spectrally hard state. This spectrally hard state can persist to high luminosities during the rise of a transient outburst. On the other hand, persistent high luminosity sources (such as LMC X-1 and LMC X-3) and transients that reach very high luminosities tend to be in spectrally soft states. Spectrally soft state transient sources tend to remain in such soft states until they reach a sufficiently low luminosity where these systems again switch to spectrally hard states (see, e.g., Figure 1 of Nowak 1995; or Figure 2 of Maccarone & Coppi 2003). Here *low* and *high* luminosity should be considered defined in terms of the black hole’s fractional Eddington luminosity. This behavior has been encapsulated in what has become known as the “*q*-diagram,” with X-ray color plotted along the horizontal axis (hard relative to soft counts increasing to the right) and X-ray count rate increasing along the vertical axis (e.g., Fender et al. 2004). Typically this diagram is plotted for a specific spacecraft, so the definitions of colors and count rates have not been universal, but characteristic patterns have emerged. It has been noted that, below $\approx 1\%$ of a source’s Eddington luminosity, black hole systems are spectrally hard and radio-loud, with the transition back to a hard state as the outburst fades occurring over a much narrower range of luminosities than the outburst-driven transition from a hard state (Maccarone 2003). Winds are seen most often in soft, bright spectral states, and their detection may even be dependent upon system inclination (Ponti et al. 2012).

To place the behavior of 4U 1957+11 in the context of such a diagram, we have analyzed the entire RXTE catalog for five black hole sources: the predominantly soft and persistent sources LMC X-1, LMC X-3, and 4U 1957+11, and the more spectrally variable sources Cyg X-1 and GX339–4, with the latter source also being transiently active. We choose these sources for several reasons. First, all have an extensive RXTE database. All have shown spectrally soft, disk-dominated states. (For the case of Cyg X-1, based upon the prior work of Wilms et al. 2006, Grinberg et al. 2014, we estimate that $\approx 6\%$ of the RXTE data points are “soft” states, and $\approx 4\%$ are “transitional” states.) The three HMXB have well-determined distances and masses, although in at least the case of LMC X-1 (see below) their HMXB nature might lead to some peculiarities in the diagram. Both 4U 1957+11 and GX339–4, however, are LMXB, and the latter source is often used as the *canonical* example of the *q*-diagram.

So as to make this diagram more *generic* for observations with other X-ray missions, we fit a simple spectral model to 3–20 keV band Proportional Counter Array (PCA) data: an absorbed disk plus broad line plus broken power law. We have previously used this model to describe phenomenologically RXTE observations of both hard and soft spectral states of Cyg X-1 (Wilms et al. 2006). We form colors by a comparison of the (absorbed) model energy fluxes in the 1.5–5 and 5–10 keV energy bands (i.e., hard minus soft rate, divided by hard plus soft rate). We choose these bands as each has good overlap with most modern X-ray and/or gamma-ray instruments (i.e., the 0.2–12 keV of NICER and the 3–70 keV of NuSTAR), and the soft band is not heavily influenced by absorption for equivalent neutral columns $N_{\text{H}} \lesssim 10^{22} \text{ cm}^{-2}$. Thus the hope is that, by using these bands, the systematic effects will be minimal when comparing results among

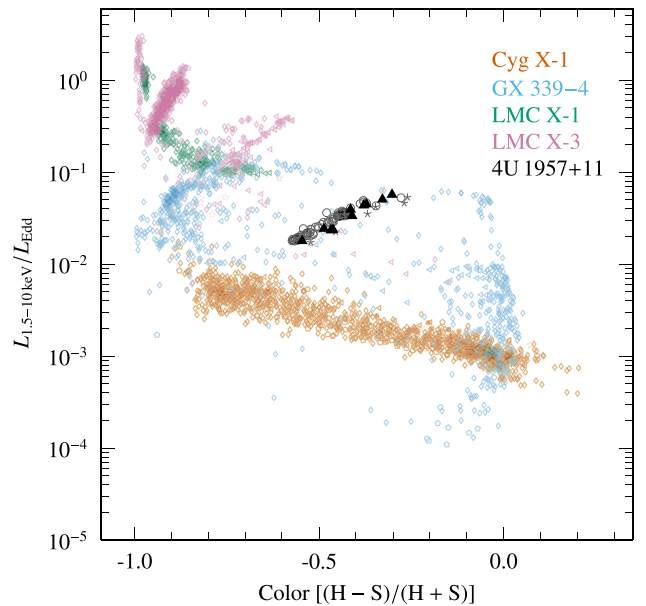


Figure 1. A *q*-diagram of intensity vs. color for RXTE observations of several different black hole candidate systems. Rather than relying on specific spacecraft observed counts, this diagram is constructed from model fits to the data, extrapolated to the 1.5–5 and 5–10 keV bands, and normalized to the Eddington ratio for assumed masses and distances (see text). Pentagons, triangles, and diamonds are for RXTE-PCA gain epochs (1), (2), and (5) (see Shaposhnikov et al. 2012, and references therein) respectively. Solid gray triangles are for our Comptonized disk fits to the NuSTAR-only spectra, and the solid gray stars are for our Comptonized disk fits to the joint NICER +NuSTAR spectra (see Section 3).

different missions. To further “normalize” the *q*-diagram, we rescale the fluxes assuming isotropic emission for assumed masses and distances: LMC X-1, $10.9 M_{\odot}$, 50 kpc (Orosz et al. 2009); LMC X-3, $7 M_{\odot}$, 50 kpc (Orosz et al. 2014); GX339–4, $5.8 M_{\odot}$, 6 kpc (Hynes et al. 2003); Cyg X-1, $21.2 M_{\odot}$, 2.22 kpc (Miller-Jones et al. 2021); and 4U 1957+11, $4.6 M_{\odot}$, 7.8 kpc (see Section 6). We then ratio this 1.5–10 keV luminosity to the Eddington luminosity for the assumed mass. The results are presented in Figure 1.

Transitions to a low luminosity, spectrally hard state at luminosities $\lesssim 1\% L_{\text{Edd}}$ are seen for LMC X-3, Cyg X-1, and GX339–4. No such evidence presents itself for 4U 1957+11 or LMC X-1. For GX339–4, LMC X-3, and to a lesser extent Cyg X-1, bright, spectrally soft states are apparent as upturns on the upper left side of the diagram, with greater extents and curvature to the right for higher fractional Eddington luminosity. The two most unusual sources in this regards are LMC X-1, which is spread predominantly horizontally along the diagram, and 4U 1957+11. LMC X-1 is already known to have slightly unusual X-ray properties for a “soft state” black hole system, e.g., peculiar correlations between normalization and temperature for disk model fits to the spectra, and high fractional variability (for a disk-dominated soft state) with little coherence between X-ray variability in the soft and hard X-ray energy bands (Nowak et al. 2001; Wilms et al. 2001). This has been attributed to the wind-fed nature of accretion in this system, which may lead to an extremely small circularization radius for the disk in this system (see the discussions in Beloborodov & Illarionov 2001; Nowak et al. 2001; Wilms et al. 2001). LMC X-3 and Cyg X-1, although also HMXB, are likely to have substantially larger disk circularization radii, and

therefore may be more likely to behave in a similar manner to an LMXB system.

On the other hand, the shape and extent of the track exhibited by 4U 1957+11 are not markedly different than the multiple soft state tracks seen for LMC X-3, or those seen for GX339–4 (and seen weakly for Cyg X-1), except for the fact that it is noticeably harder. LMC X-3, GX339–4, and Cyg X-1 only achieve such hardnesses while in or in transition to a low luminosity hard state. As we shall argue below, this unusual spectral hardness can be the result of two potential properties of 4U 1957+11: high spin and high inclination. For our hypothesized spectral model when considering NuSTAR spectra, these fit parameters are not expected to be subject to strong fitting degeneracies (Parker et al. 2019).

3. Observations

In this section, we describe the observations of 4U 1957+11 performed with several different instruments. The main focus of this paper will be on combining information from the NICER (Section 3.2; Gendreau et al. 2016) and NuSTAR (Section 3.1; Harrison et al. 2013).

As of 2022 November, there have been 10 observations of 4U 1957+11 taken with the NuSTAR observatory. The earliest of these observations was conducted quasi-simultaneously with both the X-ray Multi-Mirror Mission (XMM)-Newton and Hubble Space Telescope-Cosmic Origins Spectrograph observations. As that is a unique combination of observatories, with their own systematics to consider not represented in our other NuSTAR observations, we defer the discussion of the non-NuSTAR spectra to a future paper. (Analyses of those data, however, do not fundamentally alter any of the conclusions discussed in this work.)

Seven of the NuSTAR observations were conducted quasi-simultaneously with NICER observations. All of the NuSTAR observations showed 4U 1957+11 in a seemingly disk-dominated, spectrally soft state, as has been typical for this source. In what follows, we first consider all 10 NuSTAR observations analyzed by themselves, and then the subset of seven NuSTAR observations conducted quasi-simultaneously with NICER observations analyzed jointly as a group. We also utilize observations from MAXI (Matsuoka et al. 2009) to place our pointed observations in the context of the long-term behavior of the source.

3.1. NuSTAR Observations

The NuSTAR observatory nominally covers a range of 3–79 keV with its two focal plane module instruments (FPMA and FPMB) designed to record the energy, arrival time, and location of each incoming event. There have been ten epochs of observations of 4U 1957+11 with NuSTAR; the observation times and integrated exposures are listed in Table 1.

To process our NuSTAR observations of 4U 1957+11, we utilized the `nupipeline` and `nuproducts` tools from HEASOFT v6.29c, with standard parameter choices and filter criteria. We used calibration products current as of 2021 November (release 20211020). Spectra and lightcurves were extracted from circular regions with diameters of 50'' centered on the image of the source, while backgrounds were extracted from source-free, circular regions on the same chip with diameters of 100''. The lightcurve bin time was chosen to be 1 ms.

For spectral analyses, the pipelines created both `rmf` and `arf` standard response matrices. In all spectral analyses, we

kept the FPMA and FPMB spectra separate, but grouped them to a common energy bin grid. Specifically, we grouped the data during spectral analysis with Interactive Spectral Interpretation System (ISIS) v1.6.47 using the `group` function simultaneously applied to the FPMA and FPMB spectra. We chose a minimum combined signal-to-noise of $\sqrt{2} * 5$ per grouped bin (i.e., an average of 25 counts per bin per detector, in spectral regions with low background), and a minimum of 2–10 detector channels (increasing by 1 channel at each step) per bin at energies starting at (3, 7, 12, 19, 27, 37, 48, 61, 75) keV. The latter grouping criteria are designed to slightly oversample, but roughly follow, the detector resolution as a function of energy. The *resolution criteria* in fact dominates the binning at all but the highest energies. We then noticed bins that fully fell within the 3–100 keV range, but the final energy bin always encompassed a wide energy range with an upper value >100 keV, due to the signal-to-noise criteria, and was ignored. The upper limit of our fits therefore ranges from ≈ 20 to 70 keV.

For all figures in this work, we combine the FPMA and FPMB spectra for presentation purposes, and these spectra are shown *flux corrected* using only the NuSTAR response matrices without reference to any specific model. (Specifically, we use the ISIS `plot_unfold` function, available via the `isisscripts` package at Remeis Observatory; see the description in Nowak et al. 2005.)

3.2. NICER Observations

The NICER instrument is composed of 56 separate optics and detectors, 52 of which are operational and are used in our spectral and timing studies. It allows for very precise timing analysis with precision of better than 300 ns over the range of 0.2–12 keV. There have been fourteen individual (nonzero exposure time) epochs of observations of 4U 1957+11 taken with the NICER instrument. Seven of these epochs (several of which consist of more than one observation ID, hereafter ObsID) were performed quasi-simultaneously with NuSTAR. The dates and total integrated observing times are presented in Table 1.

In order to create “level 2” data products, the NICER data were processed with the `nicerl2` tool from HEASOFT v6.29c and the calibration database current as of 2021 November (release `xti20210707`). Default filter criteria were employed, with the exception of filtering on “undershoot” and “overshoot” events (see Gendreau et al. 2016). Prior to the release of HEASOFT v6.29c, the standard filter criteria for these values led to exclusion of a large fraction of events in a few of our observations. A modest loosening of the undershoot–overshoot limits, which has now become standard in NICER analyses, recovered a substantial number of events. The specific values that we used to filter the data are also listed in Table 1.

Additionally, we use the customized per observation (as opposed to “canned”) response matrices that became available with the HEASOFT v6.29c release, using the `nicerarf` and `nicerrmf` tools and the above cleaned event files entered as inputs. Backgrounds for the NICER observations were estimated using v5 of the `nibackgen3C50` tool. Background, however, did not play a large role in our NICER spectral analyses.

For spectral analyses, we grouped the NICER spectra based upon spectral resolution, using 1, 2, 3, 4, 5, and 6 channels per bin starting at 0.4, 1.0, 2.4, 4.0, 6.4, and 9.0 keV, respectively.

Table 1
Observation Log

Epoch	Date	NuSTAR ObsID	Start (days)	Stop (days)	GTI (ks)	NICER ObsID	Under/Over	Start (days)	Stop (days)	GTI (ks)	3–70 keV Flux (erg/cm ² /s)	Color
1	16-11-2013	30001015002	6612.65	6613.94	50.0/...	0.51×10^{-9}	Pink
2	16-9-2018	30402011002	8377.31	8378.14	37.2	1100400103	200/1.0	8378.09	8378.17	1.7	0.35×10^{-9}	Brown
3	13-3-2019	30402011004	8555.42	8556.26	33.5/...	0.87×10^{-9}	Gold
4	29-4-2019	30502007002	8602.87	8603.37	20.7	2542010101	200/1.0	8602.61	8602.94	4.5	0.55×10^{-9}	Orange
...	2542010102	200/1.0	8603.00	8603.39	3.8
5	15-5-2019	30402011006	8618.50	8619.54	37.0/...	1.15×10^{-9}	Blue
6	04-6-2019	30502007004	8638.84	8639.28	20.1	2542010201	200/1.0	8638.88	8638.98	3.8	1.10×10^{-9}	Green
...	2542010202	200/1.0	8639.02	8639.29	5.8
7	19-7-2019	30502007006	8683.26	8683.74	18.4	2542010301	200/1.0	8683.40	8683.93	14.2	1.53×10^{-9}	Cyan
8	10-9-2019	30502007008	8736.08	8736.45	10.1	2542010401	200/1.0	8736.09	8736.50	10.0	1.76×10^{-9}	Purple
9	20-10-2019	30502007010	8776.54	8776.98	19.6	2542010501	200/1.0	8776.54	8776.94	11.7	0.89×10^{-9}	Black
10	30-11-2019	30502007012	8817.88	8818.32	20.5	2542010601	300/1.5	8817.84	8817.98	4.0	0.51×10^{-9}	Magenta
...	2542010602	300/1.5	8818.03	8818.30	6.2

Note. Times refer to spacecraft times, and have not been barycenter corrected. Good time intervals (GTI) first start and final stop times are relative to Modified Julian Date 50,000, while the summed GTI exposure is given in kiloseconds. Under/over refers to the filter criteria applied to the NICER data, where the acceptable `underonly_range` was set between 0, and the given value and the acceptable `overonly_range` was set between 0 and the given value. (The related `overonly_expr` was also scaled based upon this latter upper value. Color refers to colors used (in online version) in subsequent plots.)

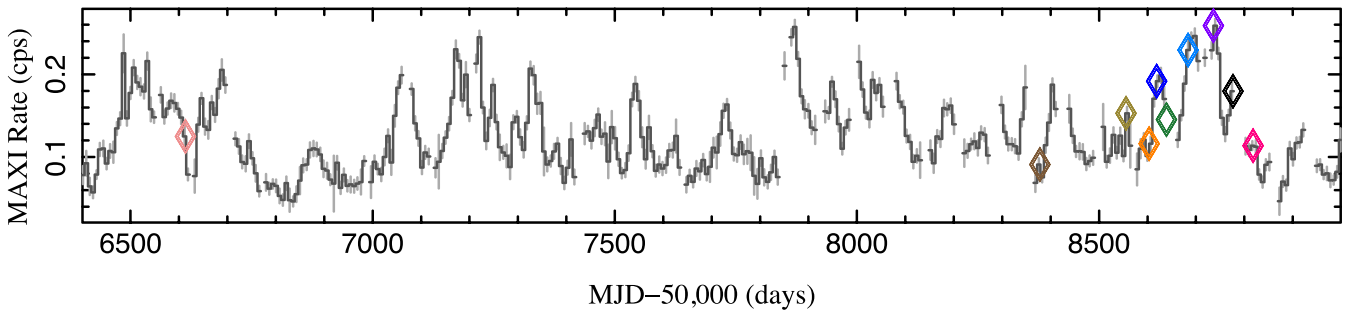


Figure 2. MAXI lightcurve for 4U 1957+11 covering a period spanning the NuSTAR/NICER observations, using 7 d bins and weighted means and 1σ error bars. Bins are included only if they are comprised of ten or more individual observations. Times, and overlapping weighted mean MAXI flux (linearly extrapolated if in a data gap), of the pointed NuSTAR observations are indicated by the hollow diamonds, color-coded (online version) to match the NuSTAR data in subsequent plots.

We included energy channels with boundaries fully within the 0.4–10 keV range. As for the NuSTAR spectra, whenever there are multiple spectra during a given epoch, we combine the NICER spectra for presentation purposes, but kept them separate during analysis.

4. Timing Analysis

4.1. Long-term Analysis—MAXI Observations

For long-term behavioral analysis of 4U 1957+11, we utilized the Monitor of All Sky X-ray Image (MAXI) 1.5 hr cadence observations, which cover an energy range of 2–20 keV. MAXI is hosted on the International Space Station, and it is composed of two semicircular X-ray cameras, a Gas Slit Camera and the Solid-state Slit Camera, and is designed to observe the sky with wide fields of view, although data gaps can occur due to blockage by the space station, the Earth, instrumental issues, etc. (Matsuoka et al. 2009). We present the 2–20 keV MAXI lightcurve in Figure 2 for the period covering our NICER and NuSTAR observations. We have binned the data into 7 day bins using an error weighted mean. We only include data bins that have at least ten contributing measurements, although we do not impose any restriction on the minimum time span covered by the measurements. We also indicate the time and overlapping weighted mean MAXI flux for the pointed NuSTAR observations. (We use a linearly extrapolated value of the MAXI flux for those NuSTAR observations that fall within a data gap.)

The lightcurves for the full MAXI lifetime (through 2022 November; not shown) span approximately a factor of 7 from the lowest to highest rates, with the extrapolated MAXI rates at the times of our NuSTAR observations spanning a factor of 2.8. Our brightest observations overlap with the highest rates observed by MAXI, and there is perhaps a further factor of 2.5 range at lower MAXI rates. Our pointed observations therefore span slightly more than half the dynamic range exhibited in the MAXI lightcurve, with approximately 23% of the MAXI bins having lower rates than those of our faintest observation. We thus have a reasonably broad and diverse sample of the historical spectral behavior exhibited by 4U 1957+11. There are no indications within the MAXI lightcurve (nor within the RXTE generated q-diagram shown in Figure 1) for a transition to a spectrally hard state at low observed rates. Given the extremely high fitted disk temperatures discussed below, such a transition could be difficult to discern solely from these color-intensity diagrams.

4.2. Short-term Analysis

We measure the fractional variability of the individual observation lightcurves via their power spectral densities (PSD), calculated via fast Fourier transforms (FFTs). We normalize these PSD following Belloni & Hasinger (1990) such that integrating over Fourier frequency yields the squared fractional variation of the counts per unit frequency.

The PSD for each NICER and NuSTAR observation was composed of an average of each of the individual PSD for the good time intervals (GTI) of each epoch of observations. The PSD were logarithmically averaged over frequencies with bins having $\Delta f/f \approx 0.08$. The most significant variability was found for the NICER lightcurves (and NICER timing analysis is more straightforward than NuSTAR timing analysis; see Bachetti et al. 2015), so here we discuss those results. The high timing precision of the NICER instrument allowed us to investigate each observation over the range of 2^{-7} –2048 Hz. We explored PSD in various energy bands, but the fractional variability was always small, and the intrinsic PSD is above the modeled Poisson noise level only in the ≈ 0.01 –0.1 Hz range. We found the highest fractional variability in the 2–8 keV band, so we discuss those results here. (Further restricting the energy band to even higher energies results in worse signal-to-noise, owing to a decrease in the NICER effective area at those energies.) We used ISIS to fit a powerlaw plus constant function (the latter to represent the PSD of the Poisson noise), with the powerlaw then being integrated over the above frequency range to measure the root mean square variability.

Overall, we found that 4U 1957+11 was remarkably quiet in all observations, with rms variabilities ranging from undetected (90% confidence upper limits of 0.7%) to 2%. The two most significant detections are for NICER ObsID 2542010201 (rms $2.0\% \pm 0.5\%$, 90% CL) and 2542010401 (rms $1.9\% \pm 0.2\%$, 90% CL). ObsID 2542010401 is among the brightest states that we observed with one of the most significant hard tails; however, ObsID 2542010201 is slightly fainter with a weaker hard tail. In all cases, however, the observed variability is modest, as shown in Figure 3. For comparison, in its soft state, Cyg X-1 can reach rms variability of up to 20% (Pottschmidt et al. 2000; Axelsson et al. 2005, 2006; Grinberg et al. 2014). In its hard state, Cyg X-1 achieves even higher rms variability of almost 40%, and has sufficient signal-to-noise so as to observe multiple Lorentzian structures in the PSD (see, e.g., Nowak 2000; Pottschmidt et al. 2003; Axelsson et al. 2005; Grinberg et al. 2014). Even with the excellent effective area of NICER, we are unable to characterize the PSD beyond a

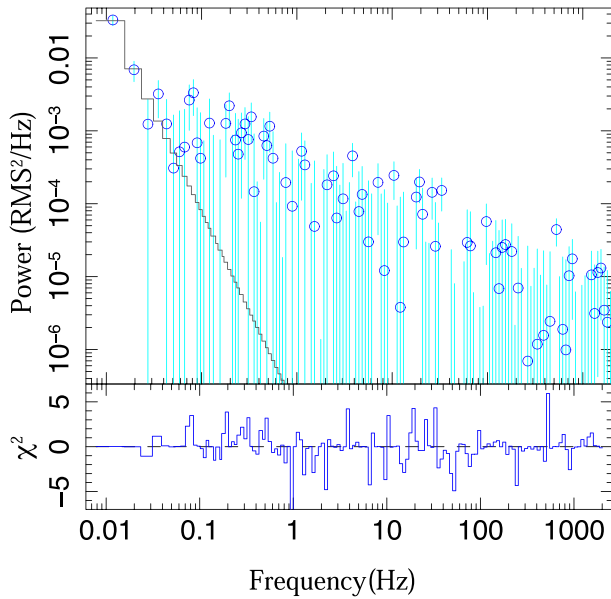


Figure 3. Power spectral density (PSD) for the 2–8 keV lightcurve of NICER ObsID 2542010401. The PSD here is fit with a constant, to describe the Poisson noise level, and a power law. The constant component has been subtracted, leaving an *upper envelope* following the expected $P(f) \propto f^{-0.5}$ residuals from Poisson noise fluctuations as high-frequency residuals. The intrinsic variability of the source is $1.9\% \pm 0.2\%$ root mean square.

simple, weak power law as has been seen historically for soft state black hole systems (e.g., Miyamoto et al. 1994).

5. Spectral Fits

Based upon prior work, we consider the fits that model the spectra as being dominated by a disk with the addition of a modest hard spectral tail. We present fits for the NuSTAR-only spectra (ten epochs) and the joint NICER/NuSTAR spectra (seven epochs). For the former, we utilize a Comptonization model with “disk” seed photons (eqpair; Coppi 1992), similar to the analysis of 4U 1957+11 presented by Nowak et al. (2012), and a relativistic disk model (polykerrbb; Parker et al. 2019, based upon kerrbb; Li et al. 2005) modified by Comptonization (thcomp; Zdziarski et al. 2020). For the joint NICER/NuSTAR spectra, we present only the thcomp@polykerrbb models. We begin, however, with a discussion of the scaling relationships we expect for the dominant disk component of the spectrum. This is an extension of previous discussions of such scaling relationships presented by Nowak et al. (2012). We modify this discussion, however, based upon the fact that the NuSTAR spectra strongly constrain both the fitted black hole spin and disk inclination for our chosen disk model, as was suggested would be the case for such high signal-to-noise and broadband spectra by Parker et al. (2019).

5.1. Scaling Relationships

Disk models—with the inclusion of components to describe a hard X-ray power-law tail—provide excellent descriptions of our data. The primary parameters of these models relate to the location of the peak of the spectrum and its overall normalization. In the models that we employ, the former is typically characterized by a color temperature, T_c , and the latter is related to the source flux, F . Color-temperature and flux are essentially *fixed* by the observations; however, their relation to physical

parameters of interest, specifically compact object mass, M , compact object spin, a^* , source distance, D , accretion disk inclination to our line of sight, i , and mass accretion rate, \dot{M} , exhibits a number of degeneracies.

In the absence of relativistic effects and when disk emission dominates the spectrum, one expects that

$$F \propto \left(\frac{R_d}{D}\right)^2 T_{\text{eff}}^4 \cos i \propto \left(\frac{M}{D}\right)^2 \left(\frac{T_c}{f_c}\right)^4 \cos i, \quad (1)$$

where R_d is a characteristic disk radius $\propto M$, and T_{eff} is the disk peak effective temperature that is related to the color temperature by a color-correction factor, f_c , with $T_c \equiv f_c T_{\text{eff}}$.

As discussed by Parker et al. (2019), and as we find below for our NuSTAR observations, broadband X-ray spectral fits potentially can strongly constrain disk inclination and spin. This is especially true for regions of parameter space that correspond to high spin and high inclination because the *width* of the temperature distribution in the disk (due to relativistic beaming and gravitational redshift) is *broadest* at high spin and inclination. The fitted *peak* of the disk temperature distribution is still highly degenerate with regards to mass, distance, accretion rate, and color-correction factor, but its breadth helps fix the spin and inclination.

We expect our spectral fits to yield $f_c \propto (M/D)^{1/2} \cos^{1/4} i$. We will show below that the fitted dependence of f_c upon $\cos i$ is predominantly systematic. That is, for a fixed, assumed (M/D) , our fit to $\cos i$ depends upon which data we include, which in turn constrains the fitted value of f_c . The dependence of f_c upon mass and distance, however, is truly degenerate in that rescaling $f_c \propto (M/D)^{1/2}$ yields exactly the same spectrum. Our spectral fits thus constrain the ratio of (M/D) only to the extent that we have independent estimates of f_c , e.g., from a theoretical prior obtained from disk atmosphere models (Davis et al. 2005, 2006; Davis & Hubeny 2006).

We can incorporate other priors to further constrain the degenerate parameters. In addition to T_c , a^* , and $\cos i$ being fixed by fits to the observation, so is the flux, F . This latter quantity can be related to the fractional Eddington luminosity as $L/L_{\text{Edd}} \propto FD^2/M$. Combining with the mass–distance dependence of the color-correction factor, we have

$$M \propto f_c^4 \frac{L}{L_{\text{Edd}}}, \quad D \propto f_c^2 \frac{L}{L_{\text{Edd}}}. \quad (2)$$

Thus priors on color-correction factor and fractional Eddington luminosity can be translated into constraints on mass and distance.

If we assume a fixed fraction of the Eddington luminosity, L/L_{Edd} , for a given observation (e.g., hypothesize that the faintest observation, not showing a spectral transition to a spectral hard state, is $\sim 0.01L_{\text{Edd}}$), we then have

$$T_c = f_c T_{\text{eff}} \propto \left(\frac{\dot{M}}{M^2}\right)^{1/4} \propto f_c \dot{M}^{1/4}. \quad (3)$$

The last proportionality is given by the assumption that $(L/L_{\text{Edd}}) \propto (\dot{M}/M)$ is fixed. Under these assumptions, because $L \propto D^2$, then $D \propto \sqrt{M} \propto \sqrt{\dot{M}}$. Spectral fits will be degenerate at constant L/L_{Edd} along lines where $M \propto D^2$, and $f_c \propto D^{1/2} \propto M^{1/4}$.

If we instead require that the color-correction factor f_c is fixed, then the fits will be degenerate along lines $M \propto D$, with

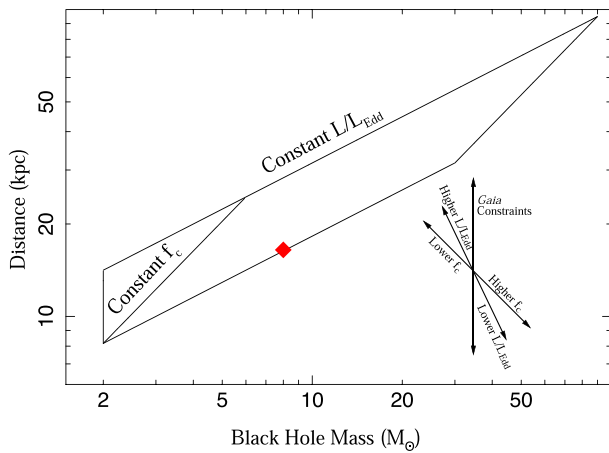


Figure 4. Lines highlighting portions of the degenerate parameter space for our spectral fits. Moves along lines of $D \propto M^{1/2}$ correspond to degenerate fits with constant L/L_{Edd} , but $f_c \propto D^{1/2} \propto M^{1/4}$. The lower of these lines corresponds to $L/L_{\text{Edd}} \approx 0.03$ for the faintest observation, while the upper line corresponds to $L/L_{\text{Edd}} \approx 0.1$ for the faintest observation. (The brightest observation is approximately 5 times brighter than the faintest observation.) For the lines of $M \propto D$, degenerate fits have constant f_c , and $L/L_{\text{Edd}} \propto M \propto D$. Moves along lines of constant M have $L/L_{\text{Edd}} \propto D^2$, and $f_c \propto D^{-1/2}$. The left vertical line at $M = 2 M_{\odot}$ corresponds to the lowest-mass one might consider for a stellar mass black hole. The red diamond corresponds to the mass and distance that we have used in our spectral fits employing disk models.

$L/L_{\text{Edd}} \propto M \propto D$. If we move along lines of constant M , then degenerate fits will scale as $L/L_{\text{Edd}} \propto D^2$, and $f_c \propto D^{-1/2}$. We illustrate these lines of degeneracy in Figure 4.

We thus only need to consider spectral fits for a single fiducial mass and distance, which leads to an assumed set of fractional Eddington luminosities and fitted probability distributions for the color-correction factor. We also obtain fitted distributions for spin and inclination, but those are independent of our assumed mass and distance, whereas the overall scale of the color-correction factor depends upon our assumptions as outlined above. To the extent that we can place priors on color-correction factor (via theoretical expectations), fractional Eddington luminosity (via comparison to other known black hole system behavior), and source distance (e.g., from Gaia measurements), we can place fit constraints on the system mass and distance.

5.2. NuSTAR-only Spectral Fits

In order to be able to directly compare results to Nowak et al. (2012), we first fit the individual NuSTAR spectra with a model that consists of interstellar absorption modifying the `eqpair` Comptonization model plus a Gaussian line, specifically `tbabs*(eqpair+Gaussian)`. The `tbabs` model is the current version from the work of Wilms et al. (2000), and we use the abundances from that work and the cross sections of Verner. Given that the equivalent neutral column along our sight line to 4U 1957+11 is small and the lower cutoff of the NuSTAR spectra is 3 keV, we fix the value to $1.7 \times 10^{21} \text{ cm}^{-2}$ (i.e., as found by Nowak et al. 2012). The Gaussian line is constrained to have an energy that lies within 6.2–6.9 keV and have a width $\sigma < 0.3$ keV, so as not to become broad and strong enough to falsely fit the continuum spectrum. For the `eqpair` model, we choose seed photons from a disk (essentially the `diskpn` model of Gierlinski et al. 1999), fix the seed photon compactness parameter to 1, and then fit the

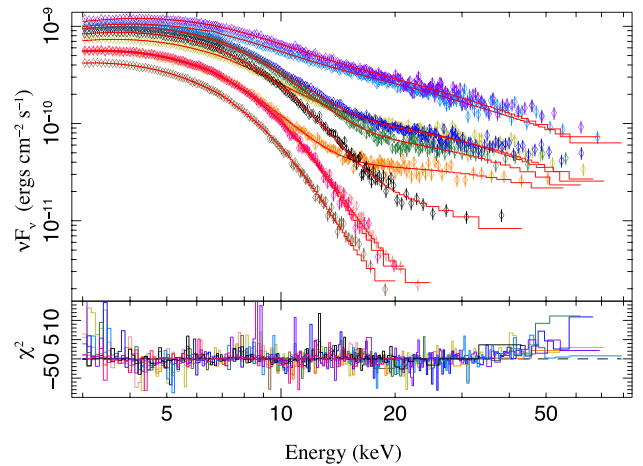


Figure 5. Flux-corrected spectra and fits, using an absorbed `eqpair` model plus relativistic reflection (see text), for NuSTAR observations of 4U 1957+11. The individual fits are independent of one another. Color-coding shown in the online color version of this figure for the individual spectra (and listed in Table 1) is used consistently in subsequent figures, e.g., showing parameter correlations.

peak disk temperature, kT_{disk} , coronal compactness parameter, l_c , and coronal seed optical depth, τ_{seed} . The `eqpair` model also provides a simple reflection model (without an Fe line), which we fit with a *reflection fraction*, R , constrained to be between 0 and 2. (This parameter is typically either weak and/or poorly constrained in our fits.) To account for differences between the two NuSTAR focal plane detectors, we introduce a cross-normalization constant by multiplying the model by $(1 \pm c_A)$, using the $+$ and $-$ for the NuSTAR-FPMA and FPMB spectra, respectively. (That is, we normalize the fits to the average of these two spectra.) Results for these fits are presented in Figure 5 and Table 2.

For these spectral fits, and all spectral fits presented in this work, parameter tables present values for the fit minimum χ^2 fits. Error bars, however, are derived from Markov Chain Monte Carlo (MCMC) analyses using an `ISIS` implementation of the `emcee` algorithms of Foreman-Mackey et al. (2013), Goodman & Weare (2010). Specifically, we evolve a group of *walkers*—in our case 5 (for the Comptonized relativistic disk fits discussed below) or 10 walkers (for these individual `eqpair` fits) per free parameter—for 20,000 steps, and create probability distributions for the parameters from the last 10,000 steps. We create one-dimensional parameter probability distributions by marginalizing over the other parameters, and then take the parameter error limits as the bounds that encompass the 90% of the probability distribution surrounding the median parameter value. (This median value could be different from the *best-fit* value, but is often nearly identical.) In some cases, the probability distributions include the fixed bounds that we have imposed (e.g., as for the Gaussian line described above), and those become part of the 90% probability bounds quoted in the tables.

These MCMC analyses have implicitly employed nonuniform priors for some of the parameters. Uniform priors only apply to those parameters directly used in the fits. In Table 2, the Compton y parameter is derived from the equilibrium coronal temperature and final electron–positron optical depth, both of which are themselves dependent upon the other fitted parameters such as disk temperature, coronal compactness, and

Table 2
Parameters for `eqpair` Fits to NuSTAR Spectra

Epoch	N_{eqp} ($\times 10^{-4}$)	kT_{disk} (keV)	l_c ($\times 10^{-2}$)	τ_{seed} ($\times 10^{-2}$)	y ($\times 10^{-2}$)	R	N_γ ($\times 10^{-4}$)	E_γ (keV)	σ_γ (keV)	c_A ($\times 10^{-2}$)	χ^2/DoF
1	$2.28^{+0.04}_{-0.04}$	$1.365^{+0.005}_{-0.007}$	$0.6^{+0.3}_{-0.1}$	$1.4^{+1.2}_{-0.6}$	$0.14^{+0.03}_{-0.03}$	$0.80^{+1.05}_{-0.74}$	$1.3^{+0.2}_{-0.4}$	$6.80^{+0.08}_{-0.15}$	$0.3^{+0.0}_{-0.1}$	$-2.7^{+0.1}_{-0.2}$	303.9/251
2	$2.20^{+0.07}_{-0.04}$	$1.279^{+0.004}_{-0.010}$	$0.3^{+0.3}_{-0.0}$	$0.2^{+1.2}_{-0.1}$	$0.07^{+0.03}_{-0.02}$	$0.84^{+1.02}_{-0.76}$	$0.6^{+0.3}_{-0.4}$	$6.90^{+0.00}_{-0.49}$	$0.3^{+0.0}_{-0.2}$	$1.9^{+0.3}_{-0.2}$	217.6/223
3	$2.51^{+0.04}_{-0.07}$	$1.410^{+0.010}_{-0.005}$	$14.7^{+0.1}_{-0.5}$	$12.3^{+0.6}_{-1.0}$	$2.22^{+0.03}_{-0.02}$	$0.06^{+0.01}_{-0.02}$	$0.7^{+0.2}_{-0.6}$	$6.90^{+0.00}_{-0.58}$	$0.3^{+0.0}_{-0.3}$	$0.0^{+0.1}_{-0.2}$	542.6/415
4	$2.31^{+0.05}_{-0.07}$	$1.348^{+0.009}_{-0.006}$	$7.1^{+0.1}_{-1.4}$	$2.6^{+0.2}_{-0.4}$	$0.85^{+0.04}_{-0.05}$	$0.15^{+0.50}_{-0.14}$	$0.6^{+0.5}_{-0.4}$	$6.53^{+0.15}_{-0.28}$	$0.0^{+0.3}_{-0.0}$	$0.5^{+0.3}_{-0.3}$	366.0/327
5	$2.48^{+0.04}_{-0.03}$	$1.529^{+0.004}_{-0.006}$	$9.2^{+0.1}_{-0.4}$	$6.2^{+0.4}_{-0.2}$	$1.38^{+0.02}_{-0.02}$	$0.02^{+0.08}_{-0.02}$	$0.9^{+0.3}_{-0.7}$	$6.90^{+0.00}_{-0.46}$	$0.3^{+0.0}_{-0.3}$	$0.5^{+0.1}_{-0.1}$	466.1/417
6	$2.47^{+0.03}_{-0.06}$	$1.528^{+0.009}_{-0.004}$	$6.7^{+0.1}_{-0.5}$	$4.3^{+0.2}_{-0.6}$	$0.99^{+0.02}_{-0.03}$	$0.05^{+0.17}_{-0.05}$	$0.6^{+0.6}_{-0.5}$	$6.46^{+0.29}_{-0.23}$	$0.1^{+0.2}_{-0.1}$	$1.3^{+0.2}_{-0.2}$	373.9/359
7	$3.21^{+0.19}_{-0.11}$	$1.434^{+0.013}_{-0.022}$	$30.7^{+0.8}_{-0.9}$	$41.7^{+4.5}_{-2.0}$	$4.50^{+0.06}_{-0.06}$	$0.02^{+0.06}_{-0.02}$	$1.7^{+0.9}_{-0.6}$	$6.66^{+0.12}_{-0.10}$	$0.0^{+0.3}_{-0.0}$	$0.6^{+0.2}_{-0.1}$	430.7/435
8	$3.13^{+0.36}_{-0.32}$	$1.491^{+0.022}_{-0.024}$	$29.2^{+0.9}_{-1.3}$	$42.8^{+5.7}_{-4.2}$	$4.36^{+0.09}_{-0.08}$	$0.02^{+0.07}_{-0.02}$	$0.3^{+1.2}_{-0.3}$	$6.66^{+0.20}_{-0.42}$	$0.0^{+0.3}_{-0.0}$	$1.1^{+9.2}_{-8.9}$	423.1/400
9	$2.29^{+0.02}_{-0.06}$	$1.512^{+0.011}_{-0.003}$	$2.0^{+0.0}_{-0.0}$	$1.7^{+0.3}_{-0.7}$	$0.28^{+0.04}_{-0.05}$	$0.57^{+1.17}_{-0.53}$	$1.8^{+0.4}_{-1.2}$	$6.59^{+0.25}_{-0.29}$	$0.3^{+0.0}_{-0.2}$	$0.0^{+0.2}_{-0.1}$	307.1/281
10	$2.19^{+0.09}_{-0.02}$	$1.376^{+0.003}_{-0.012}$	$0.3^{+0.3}_{-0.0}$	$0.2^{+1.7}_{-0.1}$	$0.07^{+0.03}_{-0.02}$	$0.82^{+1.03}_{-0.74}$	$1.5^{+0.5}_{-0.7}$	$6.39^{+0.19}_{-0.16}$	$0.3^{+0.0}_{-0.2}$	$-0.9^{+0.3}_{-0.2}$	256.0/225
All											3686.9/3333

Note. For all fits, the equivalent neutral column was frozen to $N_{\text{H}} = 1.7 \times 10^{21} \text{ cm}^2$. c_A is a cross-normalization constant such that we multiply the model by $(1 \pm c_A)$, using the + and – for the NuSTAR-FPMA and FPMB spectra respectively. Error bars are 90% confidence level.

seed optical depth. In principle one can incorporate probability priors on the independent variables so as to yield a uniform prior on the dependent variable. For the case of the Compton y parameter, this would be a complex function that would be difficult to incorporate, even numerically. Below, where we discuss how we parameterize and fit the black hole spin, the required prior is very slowly changing over the range of spins derived from the parameter posterior probability distributions, and therefore is only expected to have small impact on the final error bars.

These individual fits overall describe the NuSTAR spectra well. The fitted peak disk temperatures range from 1.28 to 1.52 keV, which are rather high values for a soft state black hole and comparable to the results presented by Nowak et al. (2012). Normalizations are also comparable to the values found by Nowak et al. (2012) and, as discussed in that work, would imply some combination of low black hole mass, large distance, high inclination, and/or high black hole spin. We find, however, more variation in the value of this normalization than those for prior studies of 4U 1957+11. Finally, the coronal component in most cases is fairly weak, as evidenced by small values of the coronal compactness parameter, l_c , as well as small values of the Compton y parameter. The latter is essentially the average change in photon energy due to Comptonization, and peaks at $\approx 5\%$ for cases where $\approx 40\%$ of the photons (based upon net coronal optical depth) undergo scattering. We discuss these results in more detail in Section 6.

We next turn to the Comptonized relativistic disk fits of the NuSTAR-only spectra. In this case, rather than fitting the spectra individually with *independent* models, we simultaneously fit all spectra with a uniform black hole mass, spin, distance, and disk inclination. Given the fit degeneracies as discussed above, we fix the black hole mass and distance to $8 M_\odot$ and 16.47 kpc,¹² but allow spin and inclination to be variable fit parameters. Rather than fit the spin directly, we fit a

dummy parameter that we tie to the spin via the relation $a^* = \tanh(p - \text{atanh}(0.998))$, such that quasi-linear changes in p lead to “interesting” changes in a^* (e.g., $a^* = 0.998$ is very different spectrally from $a^* = 0.9$, but $a^* = 0$ is not very different spectrally from $a^* = 0.1$, and we wish the fit parameter to reflect this fact across the whole range of retrograde to prograde spins; see Maitra et al. 2014). For the disk models, we further use the disk atmosphere color-correction factor as a fit parameter via direct fitting of this parameter for epoch (2), and *dummy parameters* that scale the remaining color-correction factors to this value. The only other disk parameter that varies among the individual observations is the disk accretion rate, also fit via dummy parameters that scale the accretion rates to that from epoch (2).

For the hard tail, we convolve the relativistic disk model with the `thcomp` Comptonization model (Zdziarski et al. 2020). We fix the coronal temperature to 100 keV. The remaining fit parameters for each individual observation are the hard tail photon indices, Γ_{tc} , and the corona covering factors, f_{tc} . Since we are fixing the coronal temperature (never having coverage $\gtrsim 70$ keV, and minimal spectral curvature in the hard tails at lower energies, this parameter would be very poorly constrained), f_{tc} should not be viewed as purely a covering fraction, but rather as a proxy for a combination of coronal covering fraction and optical depth.

The `eqpair` fits discussed above indicate that the iron line is weak, but plausibly present (similar to the possible detections of such a feature in the Suzaku spectra; Nowak et al. 2012). We model possible reflection and a broad iron line feature using the `relxillCp` model (Garcia et al. 2014). The `relxillCp` spin parameter is tied to the globally fit spin parameter. We tie the `relxillCp` illuminating photon index to the value of Γ_{tc} for each observation, and consider only the reflected part of the spectrum (i.e., the directly viewed hard tail only comes from the `thcomp` component). We assume that the hard tail illuminates the entire disk, and fit a single, common emissivity for all observations, which typically pegged at our imposed limit of $\epsilon_{\text{rx}} = 5$. We use an Fe abundance of $A_{\text{Fe}} = 1$. The remaining fit parameters are the `relxillCp` normalization and ionization parameters, both of which we fit for each individual observation. As for the `eqpair` fits, we incorporate

¹² Although this specific distance might at first glance seem unusual, it was chosen because, for fits using earlier versions of the NuSTAR response matrices and a subset of the spectra, this mass and distance yielded a fitted color-correction factor of 1.7 for the faintest NuSTAR observation. We in fact fit our spectra with scaling *dummy parameters* that allow us to easily replicate the degeneracies in the fits for different masses, distances, accretion rates, and color-correction factors, using the scaling relations discussed in Section 5.1.

Table 3
Global Parameters for Comptonized Disk Fits to NuSTAR and Joint NICER/NuSTAR Spectra

a^*	i ($^\circ$)	N_{H} ($\times 10^{21} \text{ cm}^{-2}$)	A_{O}	A_{Ne}	A_{Fe}	z_{NH}	x_{dust} ($\times 10^{-3}$)	ϵ_{rx}	χ^2/DoF
$0.9961^{+0.0003}_{-0.0003}$	$75.00^{+0.13}_{-0.28}$	1.7	$5.00^{+0.00}_{-0.09}$	3569.1/3351
$0.9980^{+0.0000}_{-0.0001}$	$84.05^{+0.15}_{-0.18}$	$0.95^{+0.01}_{-0.02}$	$1.3^{+0.0}_{-0.0}$	$0.0^{+0.2}_{-0.0}$	$0.3^{+0.1}_{-0.1}$	$-0.1200^{+0.0002}_{-0.0001}$	0^{+4}_{-0}	$5.00^{+0.00}_{-0.15}$	7119.3/5244

Note. All fits used $M_{\text{BH}} = 8 M_{\odot}$, and $D_{\text{BH}} = 16.47$ kpc. Likewise, the reflection models used a common power-law index, ϵ_{rx} , for the disk emissivity profiles. For NuSTAR-only fits (first entry), the equivalent neutral column was frozen to $N_{\text{H}} = 1.7 \times 10^{21} \text{ cm}^2$. For the joint NICER/NuSTAR fits (second entry), N_{H} was modeled, but with variable abundances for O, Ne, and Fe (A_{O} , A_{Ne} , A_{Fe}) and a variable redshift (z_{NH}) in order to account for possible calibration uncertainties in the NICER spectra. This absorption was modified by a dust scattering halo (see text), with the sole fit parameter being the distance from observer to halo, relative to the source distance (x_{dust}). A number of absorption lines with fixed equivalent widths, representing previously detected features (likely due to the interstellar medium; see text) were included. Error bars are 90% confidence level.

Table 4
Individual Observation Parameters for Comptonized Disk Fits to NuSTAR and Joint NICER/NuSTAR Spectra

Epoch	f_c	\dot{M} ($\times 10^{18} \text{ g s}^{-1}$)	Γ_{ic}	f_{ic}	N_{rx}	$\log \epsilon_{\text{rx}}$	c_{A} ($\times 10^{-2}$)	c_{N1} ($\times 10^{-2}$)	c_{N2} ($\times 10^{-2}$)	χ^2/DoF
1	$1.511^{+0.008}_{-0.008}$	$0.150^{+0.002}_{-0.002}$	$3.40^{+0.00}_{-0.02}$	$0.0^{+0.3}_{-0.0}$	$3.4^{+0.1}_{-0.9}$	$2.3^{+0.3}_{-0.4}$	$-2.8^{+0.2}_{-0.1}$	330.0/250
2	$1.510^{+0.008}_{-0.009}$	$0.112^{+0.002}_{-0.001}$	$3.40^{+0.00}_{-0.13}$	$0.0^{+0.4}_{-0.0}$	$1.9^{+0.0}_{-1.1}$	$2.2^{+0.3}_{-1.1}$	$1.9^{+0.3}_{-0.2}$	227.1/222
...	$1.180^{+0.006}_{-0.006}$	$0.110^{+0.001}_{-0.000}$	$2.85^{+0.17}_{-0.04}$	$0.0^{+0.8}_{-0.0}$	$0.2^{+0.0}_{-0.1}$	$1.1^{+0.2}_{-0.2}$	$1.9^{+0.3}_{-0.2}$	$-6.3^{+0.5}_{-0.6}$...	579.3/490
3	$1.475^{+0.017}_{-0.014}$	$0.175^{+0.005}_{-0.004}$	$2.62^{+0.03}_{-0.04}$	$28.7^{+1.8}_{-2.7}$	$0.3^{+0.1}_{-0.1}$	$4.1^{+0.3}_{-0.3}$	$0.0^{+0.1}_{-0.2}$	457.9/414
4	$1.487^{+0.012}_{-0.013}$	$0.145^{+0.002}_{-0.002}$	$2.26^{+0.08}_{-0.09}$	$5.5^{+1.2}_{-0.9}$	$0.1^{+0.0}_{-0.1}$	$2.7^{+0.2}_{-0.5}$	$0.5^{+0.3}_{-0.3}$	370.3/326
...	$1.148^{+0.008}_{-0.006}$	$0.144^{+0.001}_{-0.001}$	$2.44^{+0.04}_{-0.05}$	$8.3^{+0.9}_{-0.8}$	$0.2^{+0.0}_{-0.1}$	$0.8^{+0.1}_{-0.1}$	$0.5^{+0.3}_{-0.3}$	$-6.8^{+0.4}_{-0.4}$	$-6.9^{+0.4}_{-0.4}$	984.9/912
5	$1.458^{+0.009}_{-0.009}$	$0.258^{+0.003}_{-0.004}$	$2.52^{+0.05}_{-0.04}$	$15.8^{+1.3}_{-1.0}$	$0.1^{+0.2}_{-0.1}$	$2.7^{+0.7}_{-1.3}$	$0.5^{+0.1}_{-0.1}$	426.1/416
6	$1.462^{+0.012}_{-0.009}$	$0.258^{+0.003}_{-0.004}$	$2.41^{+0.08}_{-0.06}$	$10.4^{+1.3}_{-1.0}$	$0.0^{+0.0}_{-0.0}$	$4.7^{+0.1}_{-3.2}$	$1.3^{+0.2}_{-0.2}$	352.2/358
...	$1.147^{+0.008}_{-0.006}$	$0.253^{+0.002}_{-0.001}$	$2.54^{+0.03}_{-0.05}$	$11.0^{+0.8}_{-1.1}$	$0.2^{+0.0}_{-0.0}$	$0.8^{+0.0}_{-0.1}$	$1.3^{+0.2}_{-0.2}$	$-11.2^{+0.3}_{-0.3}$	$-7.7^{+0.3}_{-0.3}$	1310.6/964
7	$1.382^{+0.020}_{-0.019}$	$0.248^{+0.005}_{-0.005}$	$2.79^{+0.02}_{-0.03}$	$73.4^{+3.4}_{-3.3}$	$1.2^{+0.5}_{-0.7}$	$2.7^{+0.4}_{-0.5}$	$0.6^{+0.2}_{-0.2}$	423.9/434
...	$1.077^{+0.010}_{-0.007}$	$0.252^{+0.002}_{-0.001}$	$2.78^{+0.03}_{-0.02}$	$76.1^{+2.7}_{-2.8}$	$0.3^{+0.0}_{-0.1}$	$1.1^{+0.0}_{-0.1}$	$0.6^{+0.2}_{-0.2}$	$-6.6^{+0.2}_{-0.3}$...	1437.0/732
8	$1.422^{+0.013}_{-0.026}$	$0.269^{+0.012}_{-0.004}$	$2.79^{+0.04}_{-0.03}$	$75.1^{+4.1}_{-4.8}$	$0.8^{+0.1}_{-0.4}$	$4.3^{+0.3}_{-0.7}$	$0.6^{+0.3}_{-0.2}$	386.2/400
...	$1.043^{+0.010}_{-0.008}$	$0.290^{+0.002}_{-0.002}$	$2.85^{+0.04}_{-0.03}$	$82.9^{+4.1}_{-3.3}$	$0.3^{+0.0}_{-0.0}$	$1.1^{+0.0}_{-0.1}$	$0.6^{+0.3}_{-0.2}$	$-8.7^{+0.3}_{-0.3}$...	885.5/698
9	$1.502^{+0.011}_{-0.011}$	$0.227^{+0.003}_{-0.003}$	$3.25^{+0.10}_{-0.12}$	$1.8^{+2.1}_{-1.5}$	$7.2^{+3.7}_{-3.8}$	$1.3^{+0.4}_{-0.9}$	$0.0^{+0.2}_{-0.2}$	319.2/280
...	$1.184^{+0.008}_{-0.006}$	$0.224^{+0.002}_{-0.000}$	$2.71^{+0.07}_{-0.08}$	$2.8^{+0.8}_{-0.7}$	$0.2^{+0.0}_{-0.0}$	$0.8^{+0.1}_{-0.0}$	$0.0^{+0.2}_{-0.1}$	$-8.1^{+0.3}_{-0.3}$...	917.9/578
10	$1.510^{+0.009}_{-0.010}$	$0.151^{+0.002}_{-0.002}$	$3.39^{+0.01}_{-0.06}$	$0.0^{+0.7}_{-0.0}$	$2.4^{+0.2}_{-1.4}$	$2.0^{+0.3}_{-1.7}$	$-0.9^{+0.3}_{-0.3}$	276.5/224
...	$1.191^{+0.006}_{-0.006}$	$0.147^{+0.001}_{-0.000}$	$2.90^{+0.08}_{-0.05}$	$0.0^{+0.3}_{-0.0}$	$0.2^{+0.0}_{-0.0}$	$1.1^{+0.1}_{-0.1}$	$-0.9^{+0.3}_{-0.2}$	$-6.1^{+0.4}_{-0.4}$	$-8.0^{+0.4}_{-0.4}$	1005.1/816

Note. Degrees of freedom for each individual set of observations includes the global parameters. Three additional features (which we use to represent NICER calibration uncertainties) were added to the NICER spectra: a reverse edge, and two absorption lines. (See text.) Cross-normalization constants were added, where we multiply the model by $(1 + c_{\text{A}})$ (FPMA spectra), $(1 - c_{\text{A}})$ (FPMB spectra), or $(1 + c_{\text{N1}})$ or $(1 + c_{\text{N2}})$ (NICER spectra). Error bars are 90% confidence level.

a cross-normalization constant, c_{A} , for the FPMA and FPMB spectra. Results for these fits¹³ are presented in Tables 3 and 4.

Overall this fit is quite successful in describing all ten NuSTAR observations with a common set of black hole parameters. The spin and disk inclination, commensurate with the suggestion by Parker et al. (2019), are in fact formally strongly constrained.¹⁴ The disk accretion rates, \dot{M}_{dd} , and color-correction factors, f_c , vary for the individual observations. We have verified with various spot checks that the fits are in fact degenerate with different masses, distances, accretion rates, and color-correction factors scaling as suggested from the discussion above. Only the spin and inclination do not change among these degenerate fits, with lower spins and/or lower inclinations formally being strongly disfavored for this assumed model. The relative trends of accretion rate and disk color-

correction factor remain consistent, however, even if their absolute values change based upon assumed mass and distance. The hard tail generally increases in strength with increasing accretion rate, but the behavior is more complex than this simple statement. We discuss these issues further in Section 6.

5.3. NICER/NuSTAR Joint Spectral Fits

There are seven epochs of observations with joint NICER/NuSTAR spectra. As shown in Table 1, there is good overlap between the NICER and NuSTAR observing windows, and as discussed in Section 4, there is only a small amount of variability in the X-ray lightcurve on any timescale covered by a single observing epoch. We therefore fit the NICER and NuSTAR spectra together. NICER, however, covers a lower energy bandpass, and thus we have to include more complexity in the absorption model. Additionally, NICER is a somewhat newer instrument that is subject to greater calibration uncertainties. We account for both of these facts in our fits. For these joint fits, we present a Comptonized disk model exactly as discussed above, with the following changes to account for the NICER data.

¹³ In summary, the ISIS syntax for the fitted model follows: `tbabs (1 ± constant(1)) · (thcomp(1, polykerrbb(1)) + relxillCp(1))`, with model identifiers, e.g., the 1 here, assigned based upon observation epoch of the data set being evaluated.

¹⁴ The MCMC derived probability distribution for a^* is narrow enough such that the function of p that would yield a uniform prior on a^* does not vary strongly over that posterior range.

As for the FPMA and FPMB spectra, we introduce cross-normalization constants, c_N , for the NICER spectra. Multiplying the model by $(1 + c_N)$ essentially normalizes the NICER fit to the average of the FPMA and FPMB fits. Since the field of view of NICER is comparable to the typical size of a dust scattering halo, we apply the `xscat` dust model (Smith et al. 2016) to all spectra. We tie the neutral column to the value from the `tbabs` model (which we now allow to be a free parameter, instead of being fixed). We choose the MRN dust model for the scattering. We choose the radii of the circular extraction regions as $50''$ for the NuSTAR spectra and $180''$ for the NICER spectra. The lone fit parameter for the `xscat` dust model then becomes the distance of the halo from the observer, relative to the distance of the source, x_{dust} . This parameter was fit to be the same for all spectra.

Adding the dust model and a variable absorption to the model still leaves a number of residuals in the soft end ($\lesssim 2$ keV) of the NICER spectra. These could be a combination of the following: unmodeled ISM features, systematics in our assumed model (e.g., the assumption of an energy-independent color-correction factor, f_c for each disk spectrum, or the details of the soft excess associated with the `relxillCp` component), and/or calibration uncertainties and/or errors in the NICER response function. For ISM features, we add several fixed equivalent width absorption features using `gabs` models with fixed energies (0.530, 0.654, 0.666, 0.849, 0.855, 0.922 keV), widths (0.01 keV), and strengths to represent ISM features previously observed with the Chandra-High Energy Transmission Gratings in observations of 4U 1957+11 (Nowak et al. 2012). This still left residuals in the soft X-ray energies, some of which were alleviated by allowing the `tbabs` O, Fe, and Ne abundances and overall redshift, z_{NH} , to be free parameters. We deem these to most likely represent calibration errors in the NICER responses. Several additional features, likely due to calibration effects, were addressed by adding a *reverse edge* at ≈ 1 keV (with optical depth ≈ 0.04), and two further `gabs` absorption lines, again with widths fixed to 0.01 keV and energies of ≈ 0.572 and ≈ 0.763 keV. It should be noted that all of these features, although statistically significant owing to the high count rates of the spectra, represented only a few percent deviations from the baseline model.

Fitting this modified, Comptonized, relativistic disk model yielded good results, as seen from Tables 3 and 4, and Figure 6. Parameter trends for these fits are very similar to those for the NuSTAR-only fits, but we find that both the black hole spin and disk inclination are systematically higher, while the fitted disk color-correction factors are systematically lower.

These systematic differences between the NICER and NuSTAR spectra are most evident in the fit residuals and model components shown in Figures 6 and 7. The higher color-correction factor of the NuSTAR-only fits is apparent from the steeper high energy drop of the disk component. Likewise we see that the NuSTAR-only fits yield a steeper reflection component, although in both cases this component is weak in the Fe K band. In fact, in these models, the reflection if truly present is strongest in the $\lesssim 1$ keV NICER spectra, comprising $\lesssim 20\%$ of the flux in the 0.4–0.8 keV energy band. This soft component of the reflection model, however, is not responsible for the differences in fitted inclination and color-correction between the joint NICER/NuSTAR fits and the NuSTAR-only fits. If we restrict the NICER spectra to the 3–10 keV band, the

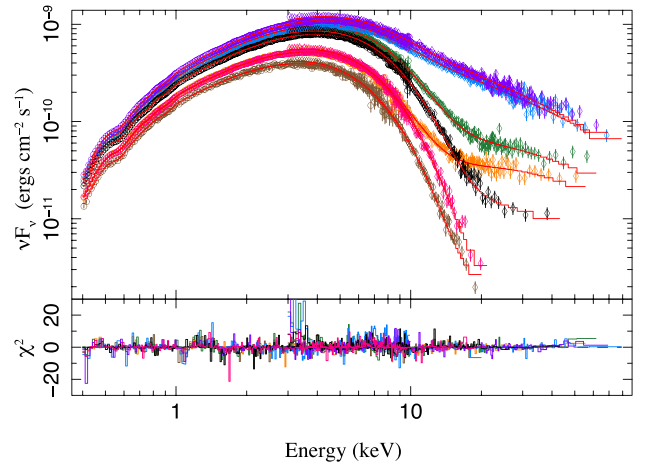


Figure 6. Flux-corrected spectra and fits using Comptonized (`thcomp`) disk atmosphere (`polykerbb`) models jointly fit to NICER/NuSTAR spectra of 4U 1957+11. The NuSTAR-FPMA and FPMB modules were fit separately, but are combined for presentation (likewise for individual NICER ObsIDs that make up an individual observing epoch).

former fits still yield the same higher inclination and lower color-correction values when compared to the NuSTAR-only fits.

If one instead postulates a *slope* difference between the NICER and NuSTAR calibrations, then altering the NICER spectra effectively by a $|\Delta\Gamma| \approx 0.03\text{--}0.07$ greatly improves the fit ($\Delta\chi^2 \approx 10^3$, when including the 0.4–10 keV NICER spectra), and drives the fitted spin, inclination, and color-correction factors closer toward the NuSTAR-only fitted values. (We do not present results from these latter fits in the remainder of this work.) We have not found any other straightforward model that improves the agreement between the NICER and NuSTAR spectra, and hypothesize that the remaining differences are dominated by systematic calibration effects.

6. Discussion

NuSTAR detects the faintest spectra of 4U 1957+11 all the way out to 20 keV, yet these spectra are nearly completely dominated by a disk spectrum with virtually no contribution from a coronal component. This is true for both the `eqpair` and Comptonized disk fits, with the fraction of scattered photons being less than half a percent (see Tables 2 and 4). At the opposite extreme, the brightest observations indicate significant scattering of the underlying disk spectra with optical depths reaching $\tau_{\text{es}} \approx 0.4$ (`eqpair` models) and covering fractions reaching $\approx 75\%$ (Comptonized disk models).

Generally, the strength of the power-law tail increases with overall flux, but there is not a single track. With the ten NuSTAR observations discussed here, there appears to be at least two tracks, both showing a hard tail increasing with rising flux, but with one having significantly stronger tails. These two tracks are quite apparent in the `eqpair` fits when plotting the Compton y value versus observed flux, as shown in Figure 8. Comparing these two tracks in terms of the long-term MAXI lightcurve presented in Figure 2, it is difficult to discern a pattern related to the 4U 1957+11 spectra being on one track versus the other.

Multiple tracks are also discernible when comparing `eqpair` normalization to observed flux, with the lowest

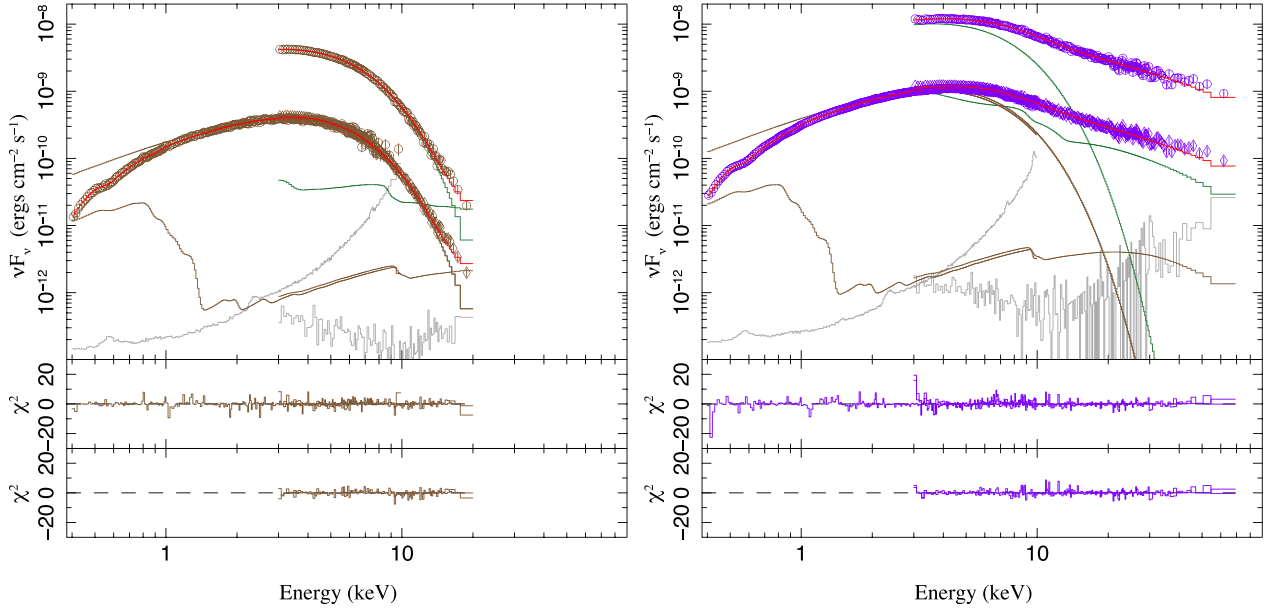


Figure 7. Flux-corrected spectra from faint (epoch (2)) and bright (epoch (8)) periods, fit with Comptonized (`thcomp`) disk atmosphere (`polykerrbb`) models see Tables 3 and 4). Here we show individual model components. For the joint NICER/NuSTAR spectra, gray lines show the background components, and brown lines show the `relxillCp` components (without absorption or other line-edge features) as well as the `polykerrbb` disk component, absent Comptonization, both with and without absorption–line-edge features included. The NuSTAR-only spectra, along with the same model components shown in green, are offset upward by a factor of 10.

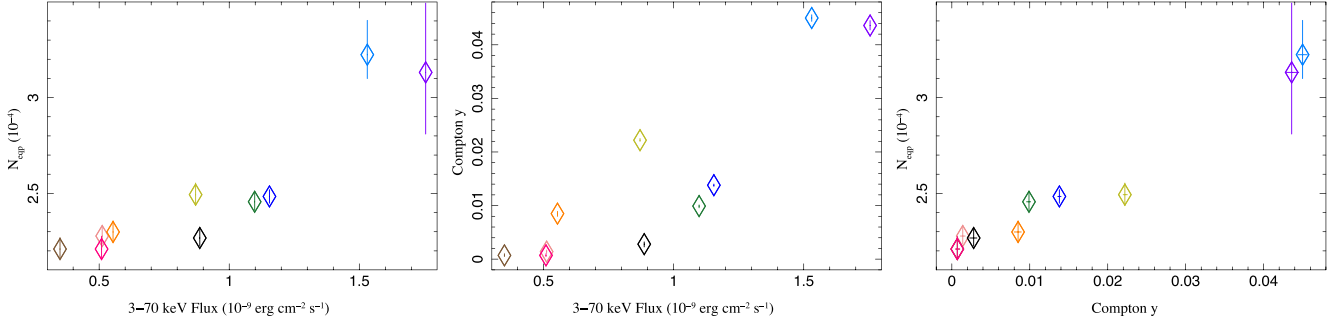


Figure 8. Correlations among parameters from `eqpair` model fits to the ten NuSTAR-only spectra. All parameters represent the best-fit values plus 90% confidence interval around the median, obtained from MCMC analyses of our best-fit models. Left: model normalization vs. absorbed 3–70 keV flux. Middle: derived Compton y parameter vs. 3–70 keV flux. Our fits always have optical depth $\tau_{\text{es}} < 1$, so $y = 4kT_e/m_e c^2 \tau_{\text{es}}$. Right: model normalization vs. Compton y parameter.

normalizations occurring at the lowest flux levels. Two-track behavior becomes less obvious when comparing `eqpair` normalization to Compton y parameter, with the lowest normalizations being associated with the smallest y parameters. The `eqpair` normalization scales as

$$N_{\text{eqp}} \propto R_{\text{in}}^2 D^{-2} f_c^{-4} \cos i, \quad (4)$$

where R_{in} is the inner disk radius (and therefore also scales with black hole mass). The increase in normalization with increasing flux therefore can be related to an increase in the inner disk radius, a decrease in color-correction factor, or a decrease in the inclination. Although changes in inclination are possible via, for example, disk warping (e.g., Pringle 1996), it would be highly unexpected to be so tightly correlated with flux, especially on these timescales. We argue below that color-correction factor changes provide the most compelling explanation.

The two-track behavior is also apparent in the Comptonized, relativistic disk fits, as shown in Figure 9. Here we show the

corona covering fractions and disk color-correction factors versus disk accretion rate. The observations with more prominent hard tails, for both NuSTAR-only and NICER/NuSTAR spectral fits, have higher coronal covering factors and lower color-correction factors. We can correlate this behavior with `eqpair` fits. The `diskpn` model that underlies the seed photon distribution for the `eqpair` model is still somewhat phenomenological compared to the `kerrbb` model at the heart of our `thcomp`⊗`polykerrbb` fits. One can imagine that the increase in `eqpair` normalization is in fact associated with a true increase in disk radius as opposed to a decrease in color-correction factor. The `kerrbb` model, on the other hand, has a fixed inner radius in geometrical units of GM_{BH}/c^2 , and attempts to fit the black hole spin, disk inclination, and accretion rate based upon both the energy of the spectral peak and the breadth of this peak. It is the breadth of this peak, more precisely measured with these NuSTAR spectra than for any previous observations of 4U 1957+11, that leads to such a strong constraint on fitted spin and disk inclination as these spectra are in the least degenerate portion of parameter space

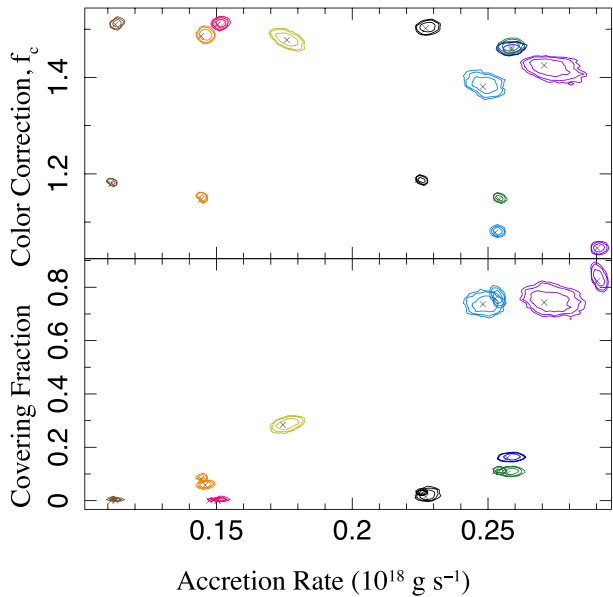


Figure 9. Correlations from `thcomp@polykerrbb` model fits to the NuSTAR-only spectra and NICER/NuSTAR spectra. We show 68%/90%/95% confidence intervals obtained from MCMC analyses of our best fits. Top panel: disk color-correction factors vs. accretion rate. The NuSTAR-only spectra yield the higher color-correction factors. Bottom panel: Compton corona covering fraction vs. disk accretion rate. The NuSTAR-only spectra yield the broader confidence contours.

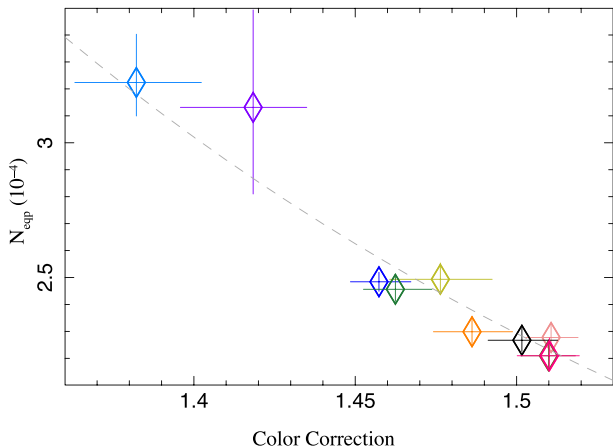


Figure 10. Model normalization for `eqpair` model vs. color-correction factor for Comptonized (`thcomp`) disk atmosphere (`polykerrbb`) model fits to NuSTAR-only spectra of 4U 1957+11. The dashed line shows scaling the normalization $\propto f_c^{-4}$.

for our assumed model (Parker et al. 2019). Correlating the `eqpair` normalizations with the Comptonized relativistic disk color-corrections, we see in Figure 10 that the normalizations follow the f_c^{-4} behavior expected if only this latter parameter, and not the disk inner radius, varies. The fact that the `thcomp@polykerrbb` fits, which again postulate an unchanging inner disk radius, provide excellent fits at least in the NuSTAR-only case argues strongly for color-correction changes dominating.

Disk color-corrections are essentially due to electron scattering in the upper atmosphere of the disk (Davis et al. 2005). We thus are drawn to a scenario where as electron scattering is increased in a hot corona it is decreased in the upper atmosphere of the optically thick accretion disk itself.

What are we to then make of the systematic difference between the fitted color-correction factor for the NuSTAR-only and NICER/NuSTAR fits? We hypothesize that this is predominantly a systematic effect owing to calibration error in one or both of NuSTAR and NICER. Spin and inclination estimates, especially at these high fitted values, are strongly driven by the *breadth* of the spectral peak. A high spin, near edge-on disk has a very broad spectral peak because we are seeing both extreme red and blueshifts of the disk spectrum. The NICER spectra, as discussed above for the `eqpair` fits, show a spectral hardening compared to NuSTAR of $|\Delta\Gamma| \approx 0.03\text{--}0.07$. The peak of the NICER spectra is *broader* than that seen by NuSTAR, and therefore the disk must be more highly inclined to fit the spectrum. The peak of the spectrum, however, is not changed (leading to a similar accretion rate for a given assumed mass), and the overall flux must remain unchanged; therefore the color-correction factor must drop to compensate for the higher inclination. The ratio of fitted color-correction factors between the two sets of fits is in fact almost exactly given by the ratio of the cosine of the fitted disk inclination angles as expected for this systematic dependence.

Of the two fitted values, the NuSTAR-only value of $i \approx 75^\circ$ is more plausible, as the NICER/NuSTAR value of $i \approx 84^\circ$ should have led to discernible eclipsing of the disk. A 75° inclination will not lead to an eclipse of the primary by the Roche lobe of the secondary if the primary mass is $\gtrsim 2 M_\odot$ (for a $0.5 M_\odot$ secondary) or is $\gtrsim 4 M_\odot$ (for a $1 M_\odot$ secondary). These values increase to $\gtrsim 50 M_\odot$ and $\gtrsim 160 M_\odot$, respectively, for an 85° inclination. This is ignoring any warp or raised edge and/or atmosphere in the outer disk, which could lead to quasi-periodic obscuration at lower inclination angles, as has been observed in the so-called “dipping” sources (e.g., 4U 1624–490; Xiang et al. 2007). It is debatable whether or not dipping should be observed in 4U 1957+11 if the inclination is $\approx 75^\circ$. Although dipping has been observed in systems with likely lower inclination angles, its presence or absence can be spectrally dependent (e.g., XB 1254–690; Díaz Trigo et al. 2009). Furthermore, Galloway et al. (2016) argue that $i \lesssim 75^\circ$ is a plausible typical inclination angle demarcating the boundary between sources that are intermittently dipping from those that never exhibit dipping. We hypothesize that the NuSTAR spectral calibration is closer to *accurate* compared to the NICER spectral calibration, although we cannot discount the possibility that revisions to both calibrations would lead to best fits with $i < 75^\circ$.

This lack of fit-degeneracies in terms of spin and inclination, but remaining degeneracies for mass, distance, and color-correction factor, as well as the variation of `eqpair` normalization, is somewhat counter to the previous Swift (Maitra et al. 2014), Suzaku (Nowak et al. 2012), and RXTE (Nowak & Wilms 1999) studies of 4U 1957+11. We note, however, that studies with Swift and Suzaku were limited to energies $\lesssim 10$ keV, while studies with RXTE had hard X-ray backgrounds approximately 100 times greater than for these NuSTAR spectra, with corresponding lower signal-to-noise in the hard tail. NuSTAR is the first instrument to be able to accurately characterize the hard tail and thereby accurately characterize the breadth of the disk spectrum peak. For example, for the faintest NuSTAR spectra with the weakest hard tails, the nearly pure disk spectrum is measured out as far as 20 keV.

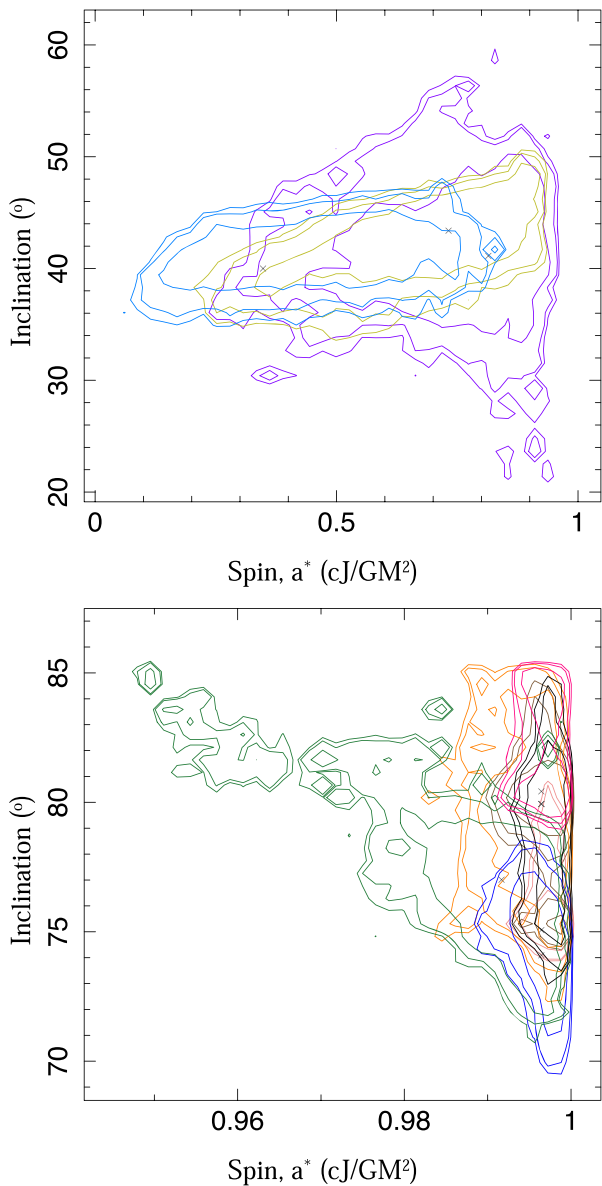


Figure 11. Contours of fitted spin vs. inclination, if we allow independent spins and inclinations for Comptonized (`thcomp`) disk atmosphere (`polykerrbb`) model fits to NuSTAR-only spectra of 4U 1957+11. The top figure shows the contours for the three spectra with the strongest hard tails, while the bottom panel shows the contours for the remaining observations.

We can also ask to what extent our results are driven by systematics of our model assumptions, and whether or not individual fits support the same results as our *global model* with fixed black hole spin and inclination. The fact that the individually fit `eqpair` models yield the same trends, e.g., for color-correction versus hard tail strengths, as our global model gives us optimism that we are detecting robust, physically meaningful trends. Likewise, we note that if we relax the assumption of a common disk inclination for the observations, the NuSTAR-only spectral fit improves by only $\Delta\chi^2 \approx 7$ (for 9 additional parameters), with the individual fitted inclinations varying from the globally fit value by $\lesssim 1^\circ$.

If we let both spin and inclination be free for each observation, we find $\Delta\chi^2 \approx 69$ (for 18 additional parameters) compared to the NuSTAR-only global model. Almost all of this improvement comes from epochs (3), (7), and (8), where

formally a better fit is found with disk inclinations $\approx 40^\circ$, spin parameters ranging from $a^* \approx 0.3$ to 0.9, and extremely large color-correction factors $f_c \approx 4.4$ –4.8. We show the error contours (derived from MCMC analyses) for spin versus inclination for these fits in Figure 11. The three observations that fit lower inclinations and spins exhibit the strongest fitted coronal components in all of our hypothesized models. The remaining seven observations have inclination, spin, and color-correction values comparable to the global fit values. Despite extensive searches across the parameter space, we have not found any statistically preferred low inclination, low spin solutions for these latter observations with weaker fitted coronal components. We note, however, for the discussion that follows, that such solutions, if they do exist, would also require higher fitted color-correction factors. This in turn would drive the posterior estimates on mass to lower values and the posterior estimates on distance to higher values. (See Figure 4 and the discussion below.)

The statistical uncertainties in our fits are small; uncertainties in fit parameters are dominated by the systematics of the instrument calibrations, the fidelity of our assumed model to the physical truth, and our prior beliefs as to the most *reasonable* parameter values. Here we use the scaling relations of Section 5.1 to combine our best-fit parameters with specific prior probabilities to derive probability distributions for the mass of and distance to 4U 1957+11 in the context of our assumed disk model. We use an updated version (P. Gandhi 2022, private communication) of the Gaia EDR3 distance probability distribution from Maccarone et al. (2020), which accounted for the fact that 4U 1957+11 likely lies in the Galactic halo. This probability distribution peaks at 6 kpc but still has significant cumulative probability (17%) in the 15–30 kpc range. For the color-correction factor, we choose a Gaussian prior centered on $f_c = 1.7$, with $\sigma = 0.1$. Finally, we choose a prior on the fractional Eddington luminosity for the *faintest* of our observations that is 0 at $L \leq 0.005 L_{\text{Edd}}$, and $L \geq 0.08 L_{\text{Edd}}$, linearly rising between 0.005 and 0.02 L_{Edd} , flat from 0.02 to 0.04 L_{Edd} , and then linearly falling between 0.04 and 0.08 L_{Edd} . For the brightest observation, multiply these values by approximately 5. The concept here is that if the faintest observation were much fainter (in terms of fractional Eddington luminosity), and 4U 1957+11 is a black hole, then we would have observed a transition to the hard state. If the brightest observation were much brighter, we likely would have detected greater X-ray variability, especially given the significant hard tail seen in our brightest observations. Combining these distributions with the scaling relations of Section 5.1 and our best-fit values for the Comptonized, relativistic disk fits, we arrive at the probability distributions shown in Figure 12.

Given these assumptions, for the NuSTAR-only fits, then the peak of the mass–distance probability distribution is at $M = 4.6 M_\odot$, and $D = 7.8$ kpc, with 50% of the marginalized mass distribution being at $M < 7.2 M_\odot$. A substantial portion of the mass probability distribution (22%) lies within the *mass gap* of ≈ 2 – $5 M_\odot$, although higher masses–larger distances do still easily fit within the posterior probability. Considering instead a luminosity–color-correction posterior probability, the peak of the distribution (for the faintest observation) is at $L/L_{\text{Edd}} \approx 0.017$, which would then imply the brightest observation is at $L/L_{\text{Edd}} \approx 0.09$. These values reasonably would allow for a factor of approximately 2 fainter state than

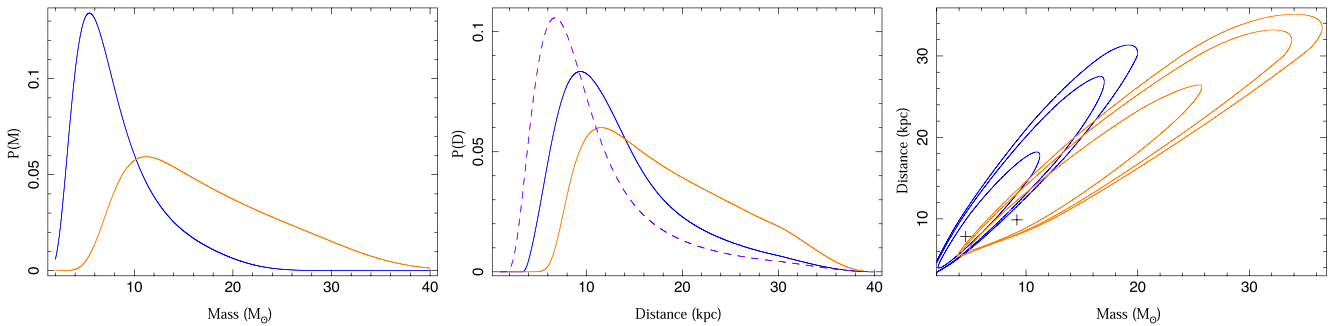


Figure 12. Probability distributions for black hole mass (left) and distance (middle) and contours of mass vs. distance (right) based upon the NuSTAR-only fits (blue lines, leftmost peaks) and the joint NICER-NuSTAR fits (orange lines, rightmost peaks) of the flux and color-correction factor for Comptonized, relativistic disk models of 4U 1957+11. The dashed purple line represents the Gaia EDR3 derived probability distribution for the distance to the 4U 1957+11 system. As described in the text, the other inputs to these curves were assumed distributions for the preferred disk atmosphere model color-correction factor and fractional Eddington luminosity ratios for 4U 1957+11.

our faintest NuSTAR observation to exist in the MAXI timeline, without having exhibited evidence for a transition to a spectrally hard state. The marginalized luminosity distribution (not shown) is essentially 0 at values $L/L_{\text{Edd}} \gtrsim 0.06$ for the faintest observation, which implies an upper limit of $L/L_{\text{Edd}} \lesssim 0.3$ for the brightest observation.

7. Summary and Conclusions

In summary, for these newest X-ray observations of 4U 1957+11 a relativistic disk, with low absorption column and a modest hard tail, describe the spectra extremely well. The lack of any extra components for *surface emission*, and no historical evidence of either bursts or pulsar periods, has made a neutron star hypothesis less favored. For the black hole Comptonized disk models that we have explored, the hard tail is nearly completely absent in the faintest spectra, yet NuSTAR detects the spectra out to 20 keV. The tail does increase with increasing accretion rate, but there are at least two tracks for this behavior, with one exhibiting a much stronger hard tail than the other (e.g., compare observations from epochs (4) and (9)). A strong correlation is seen between the increase of the hard tail (regardless of track) and decrease of color-correction factor in the disk. None of these observations exhibit significant short-term variability.

The spectral fits strongly constrain the allowed spin and inclination of 4U 1957+11 given our assumed disk model. Uncertainties in these parameters are almost wholly systematic in nature and are related to the fidelity with which our assumed model describes the underlying physical truth as well as the accuracy of the instrumental calibrations. These latter concerns mostly affect the fitted inclination, which in turn systematically alters the disk color-correction factor. All models that we have explored wherein we apply a uniform spin for all observations yield best-fit disk spectra for a near maximally spinning black hole.

Allowing spins and inclinations to vary among fits to individual epochs only modestly improves the statistics of the fits with only three of the observations fitting lower inclinations and spins, but with substantially higher color-correction factors. These three spectra also have the largest contributions from coronal components in the context of our assumed models. If these solutions are more indicative of the underlying true system parameters, decreasing the fitted color-correction fractions, while ensuring that the implied luminosities do not fall within a low fractional Eddington range that likely would

have led to an observed spectrally hard state, would push the 4U 1957+11 mass lower and distance higher in our posterior estimates. That is, an extremely low mass black hole (or high-mass neutron star) would become more likely. This remains perhaps one of the greater concerns in our modeling, i.e., that we have failed to discover a Comptonization scenario that mimics the high spin–high inclination fits of our disk-dominated models.

That being said, we find the NuSTAR-only fits to provide a believable inclination solution, consistent with the lack of any observed eclipses by the Roche lobe of the secondary, and plausibly consistent with the lack of dips (but on the cusp of where such dips might be expected to occur). The higher inclination found in the NICER +NuSTAR fits would lead to eclipses by the secondary unless the primary mass was extremely large. Adding in plausible observational priors (on fractional Eddington luminosity and distance) plus theoretical priors (on color-correction factor) constrains the resulting mass–distance relation to a narrow strip, albeit one that still covers a wide range of masses and distances. A large fraction of the probability distribution, however, resides in the *mass gap* of $2\text{--}5 M_{\odot}$. If one could confirm the suggested mass ratio of $0.25\text{--}0.3$ (Longa-Peña 2015), then these fits would be consistent with a black hole of mass $\lesssim 4 M_{\odot}$ and distance < 10 kpc. Improving those optical measurements, however, remains extremely challenging for the 4U 1957+11 system.



We thank Poshak Gandhi for providing the Gaia EDR3 probability distribution for the distance to 4U 1957+11. We acknowledge useful conversations with Tom Maccarone and Jim Buckley, and also with members of the NuSTAR X-ray Binaries working group. We thank the referee for comments that improved this manuscript. This research has made use of MAXI data provided by RIKEN, JAXA, and the MAXI team. Additionally, this research has made use of a collection of ISIS functions (*isisscripts*) provided by ECAP/Remeis observatory and MIT.¹⁵ This work has been supported by both the NuSTAR Guest Observer Program via JPL contract 1617863 and the NICER Guest Observer Program via NASA grant 80NSSC19K1583. Erin Barillier also gratefully acknowledges the support of the McDonnell Center for the Space Sciences at Washington University in Saint Louis and support from the Baines Family Planetary Science Scholarship, made possible by Dr. Kevin H. Baines, Physics PhD.

¹⁵ <http://www.sternwarte.uni-erlangen.de/isis/>

Facilities: Gaia, MAXI, NICER, NuSTAR.

Software: HEASOFT v6.29c (HEASARC 2021), XSPEC v12.11.1 (Arnaud 1996), RELXILL v1.2.0 (Garcia et al. 2014), ISIS v1.6.2-47 (Houck & Denicola 2000).

ORCID iDs

Erin Barillier  <https://orcid.org/0000-0001-9107-6542>
 Victoria Grinberg  <https://orcid.org/0000-0003-2538-0188>
 David Horn  <https://orcid.org/0000-0002-6288-4791>
 Michael A. Nowak  <https://orcid.org/0000-0001-6923-1315>
 Ronald A. Remillard  <https://orcid.org/0000-0003-4815-0481>
 James F. Steiner  <https://orcid.org/0000-0002-5872-6061>
 Dominic J. Walton  <https://orcid.org/0000-0001-5819-3552>
 Jörn Wilms  <https://orcid.org/0000-0003-2065-5410>

References

- Arnaud, K. A. 1996, in ASP Conf. Ser. 101 *Astronomical Data Analysis Software and Systems V*, ed. G. H. Jacoby & J. Barnes (San Francisco, CA: ASP), 17
- Axelsson, M., Borgonovo, L., & Larsson, S. 2005, *A&A*, 438, 999
- Axelsson, M., Borgonovo, L., & Larsson, S. 2006, *A&A*, 452, 975
- Bachetti, M., Harrison, F. A., Cook, R., et al. 2015, *ApJ*, 800, 109
- Bayless, A. J., Robinson, E. L., Mason, P. A., & Robertson, P. 2011, *ApJ*, 730, 43
- Belloni, T., & Hasinger, G. 1990, *A&A*, 227, L33
- Beloborodov, A. M., & Illarionov, A. F. 2001, *MNRAS*, 323, 167
- Coppi, P. S. 1992, *MNRAS*, 258, 657
- Davis, S. W., Blaes, O. M., Hubeny, I., & Turner, N. J. 2005, *ApJ*, 621, 372
- Davis, S. W., Done, C., & Blaes, O. M. 2006, *ApJ*, 647, 525
- Davis, S. W., & Hubeny, I. 2006, *ApJS*, 164, 530
- Díaz Trigo, M., Parmar, A. N., Boirin, L., et al. 2009, *A&A*, 493, 145
- Farr, W. M., Sravan, N., Cantrell, A., et al. 2011, *ApJ*, 741, 103
- Fender, R. P., Belloni, T. M., & Gallo, E. 2004, *MNRAS*, 355, 1105
- Foreman-Mackey, D., Hogg, D. W., Lang, D., & Goodman, J. 2013, *PASP*, 125, 306
- Gaia Collaboration, Brown, A. G. A., Vallenari, A., et al. 2021, *A&A*, 649, A1
- Gaia Collaboration, Prusti, T., de Bruijne, J. H. J., et al. 2016, *A&A*, 595, A1
- Galloway, D. K., Ajamyan, A. N., Upjohn, J., & Stuart, M. 2016, *MNRAS*, 461, 3847
- García, J., Dauser, T., Lohfink, A., et al. 2014, *ApJ*, 782, 76
- Gendreau, K. C., Arzoumanian, Z., Adkins, P. W., et al. 2016, *Proc. SPIE*, 9905, 99051H
- Gierlinski, M., Zdziarski, A. A., Poutanen, J., et al. 1999, *MNRAS*, 309, 496
- Giesers, B., Dreizler, S., Husser, T.-O., et al. 2018, *MNRAS*, 475, L15
- Giesers, B., Kamann, S., Dreizler, S., et al. 2019, *A&A*, 632, A3
- Gomez, S., Mason, P. A., & Robinson, E. L. 2015, *ApJ*, 809, 9
- Goodman, J., & Weare, J. 2010, *CAMCS*, 5, 65
- Grinberg, V., Hell, N., Pottschmidt, K., et al. 2013, *A&A*, 554, A88
- Grinberg, V., Pottschmidt, K., Böck, M., et al. 2014, *A&A*, 565, A1
- Hakala, P., Muhli, P., & Charles, P. 2014, *MNRAS*, 444, 3802
- Hakala, P. J., Muhli, P., & Dubus, G. 1999, *MNRAS*, 306, 701
- Harrison, F. A., Craig, W. W., Christensen, F. E., et al. 2013, *ApJ*, 770, 103
- Houck, J. C., & Denicola, L. A. 2000, in ASP Conf. Ser. 216, *Astronomical Data Analysis Software and Systems IX*, ed. N. Manset, C. Veillet, & D. Crabtree (San Francisco, CA: ASP), 591
- Hynes, R. I., Steeghs, D., Casares, J., Charles, P. A., & O'Brien, K. 2003, *ApJL*, 583, L95
- Li, L.-X., Zimmerman, E. R., Narayan, R., & McClintock, J. E. 2005, *ApJS*, 157, 335
- Longa-Peña, P. 2015, PhD thesis, Univ. Warwick
- Maccarone, T. J. 2003, *A&A*, 409, 697
- Maccarone, T. J., & Coppi, P. S. 2003, *MNRAS*, 338, 189
- Maccarone, T. J., Osler, A., Miller-Jones, J. C. A., et al. 2020, *MNRAS*, 498, L40
- Maitra, D., Miller, J. M., Reynolds, M. T., Reis, R., & Nowak, M. 2014, *ApJ*, 794, 85
- Margon, B., Thorstensen, J. R., & Bowyer, S. 1978, *ApJ*, 221, 907
- Mason, P. A., Robinson, E. L., Bayless, A. J., & Hakala, P. J. 2012, *AJ*, 144, 108
- Matsuoka, M., Kawasaki, K., Ueno, S., et al. 2009, *PASJ*, 61, 999
- Miller-Jones, J. C. A., Bahramian, A., Orosz, J. A., et al. 2021, *Sci*, 371, 1046
- Mitsuda, K., Inoue, H., Koyama, K., et al. 1984, *PASJ*, 36, 741
- Miyamoto, S., Kitamoto, S., Iga, S., Hayashida, K., & Terada, K. 1994, *ApJ*, 435, 398
- Mudambi, S. P., Gudennavar, S. B., Misra, R., & Bubbly, S. G. 2022, *MNRAS*, 517, 4489
- Nowak, M. A. 1995, *PASP*, 107, 1207
- Nowak, M. A. 2000, *MNRAS*, 318, 361
- Nowak, M. A., Juett, A., Homan, J., et al. 2008, *ApJ*, 689, 1199
- Nowak, M. A., & Wilms, J. 1999, *ApJ*, 522, 476
- Nowak, M. A., Wilms, J., & Dove, J. B. 1999, *ApJ*, 517, 355
- Nowak, M. A., Wilms, J., Heindl, W. A., et al. 2001, *MNRAS*, 320, 316
- Nowak, M. A., Wilms, J., Heinz, S., et al. 2005, *ApJ*, 626, 1006
- Nowak, M. A., Wilms, J., Pottschmidt, K., et al. 2012, *ApJ*, 744, 107
- Orosz, J. A., McClintock, J. E., Remillard, R. A., & Corbel, S. 2004, *ApJ*, 616, 376
- Orosz, J. A., Steeghs, D., McClintock, J. E., et al. 2009, *ApJ*, 697, 573
- Orosz, J. A., Steiner, J. F., McClintock, J. E., et al. 2014, *ApJ*, 794, 154
- Parker, M. L., Buisson, D. J. K., Tomsick, J. A., et al. 2019, *MNRAS*, 484, 1202
- Ponti, G., Fender, R. P., Begelman, M. C., et al. 2012, *MNRAS*, 422, L11
- Pottschmidt, K., Wilms, J., Nowak, M. A., et al. 2000, *A&A*, 357, L17
- Pottschmidt, K., Wilms, J., Nowak, M. A., et al. 2003, *A&A*, 407, 1039
- Pringle, J. E. 1996, *MNRAS*, 281, 357
- Ricci, D., Israel, G. L., & Stella, L. 1995, *A&A*, 299, 731
- Romani, R. W., Kandel, D., Filippenko, A. V., Brink, T. G., & Zheng, W. 2022, *ApJL*, 934, L17
- Russell, D. M., Lewis, F., Roche, P., et al. 2010, *MNRAS*, 402, 2671
- Russell, D. M., Miller-Jones, J. C. A., Maccarone, T. J., et al. 2011, *ApJL*, 739, L19
- Shaposhnikov, N., Jahoda, K., Markwardt, C., Swank, J., & Strohmayer, T. 2012, *ApJ*, 757, 159
- Sharma, P., Sharma, R., Jain, C., Dewangan, G. C., & Dutta, A. 2021, *RAA*, 21, 214
- Shenar, T., Sana, H., Mahy, L., et al. 2022, *A&A*, 665, A148
- Smith, R. K., Valencic, L. A., & Corrales, L. 2016, *ApJ*, 818, 143
- Thompson, T. A., Kochanek, C. S., Stanek, K. Z., et al. 2020, *Sci*, 368, eaba4356
- Thompson, T. A., Kochanek, C. S., Stanek, K. Z., et al. 2019, *Sci*, 366, 637
- Thorstensen, J. R. 1987, *ApJ*, 312, 739
- Wijnands, R., Miller, J. M., & van der Klis, M. 2002, *MNRAS*, 331, 60
- Wilms, J., Allen, A., & McCray, R. 2000, *ApJ*, 542, 914
- Wilms, J., Nowak, M., Pottschmidt, K., Pooley, G. G., & Fritz, S. 2006, *A&A*, 447, 245
- Wilms, J., Nowak, M. A., Pottschmidt, K., et al. 2001, *MNRAS*, 320, 316
- Xiang, J., Lee, J. C., & Nowak, M. A. 2007, *ApJ*, 660, 1309
- Yao, Y., Nowak, M. A., Wang, Q. D., Schulz, N. S., & Canizares, C. R. 2008, *ApJL*, 672, L21
- Yaqoob, T., Ebisawa, K., & Mitsuda, K. 1993, *MNRAS*, 264, 411
- Zdziarski, A. A., Szanecki, M., Poutanen, J., Gierliński, M., & Biernacki, P. 2020, *MNRAS*, 492, 5234